

INVESTIGATING SUBSTRUCTURE FLEXIBILITY IN COLUMN-TOP
ISOLATION SYSTEMS WITH ELASTOMERIC BEARINGS

INVESTIGATING SUBSTRUCTURE FLEXIBILITY IN COLUMN-TOP
ISOLATION SYSTEMS WITH ELASTOMERIC BEARINGS

By
ADRIAN P. CROWDER, B. Eng.

A Thesis Submitted to the School of Graduate Studies in Partial Fulfilment of the
Requirements for the Degree Master of Applied Science

McMaster University
© Copyright by Adrian P. Crowder, June 2016

MASTER OF APPLIED SCIENCE (2016)

(Civil Engineering)

McMaster University

Hamilton, Ontario

TITLE: Investigating Substructure Flexibility in Column-Top
Isolation Systems with Elastomeric Isolation Bearings

AUTHOR: Adrian P. Crowder, B.Eng. (McMaster University)

SUPERVISOR: Dr. Tracy C. Becker

NUMBER OF PAGES: xi, 96

ABSTRACT

Seismic isolation is a method of earthquake resistant design which has been proven to effectively reduce the damaging effects of earthquakes on buildings as well as the contents within them. However, traditional implementation of an isolation system tends to be expensive. For new construction, rigid diaphragms above and below the isolation layer and construction of a seismic gap contribute to expenses, while retrofit applications also require excavation beneath the building and may need extensive foundation work. To mitigate these major costs bearings may be placed on the tops of columns, forgoing the construction of a seismic gap, additional rigid diaphragm, and foundation work. However, columns under the isolation layer may be flexible, changing the bearing end conditions traditionally assumed.

To investigate the effects of flexible end conditions on elastomeric bearings, an analytical model that accounts for translation and rotation of both endplates was developed based on Haringx's theory. The derivation accounts for compressibility of the rubber and results in a simple stiffness matrix. To evaluate the model, an experimental program testing column-bearing subassemblies under quasi-static cyclic conditions was conducted. Experimental findings show that flexible end conditions can significantly reduce the lateral stiffness of elastomeric bearings. Simulations with the theoretical model compare well under small deformations, but elastic softening of the moment-rotation relationship causes theoretical results to diverge from experimental with larger endplate rotations.

The effectiveness of column-top isolation as a retrofit strategy was investigated through nonlinear time history analyses of a moment resisting frame designed to the 1965 National Building Code of Canada and retrofitted with column-top isolation. The frame was simulated under ground motions representative of current hazards and showed that the retrofit resulted in significant reductions in interstory drifts and floor accelerations. Yielding was observed throughout the original frame under maximum considered earthquakes, while the retrofit frame remained elastic.

ACKNOWLEDGEMENTS

Firstly, I would like to acknowledge my supervisor, Dr. Tracy Becker, for the many opportunities given to me during the course of this research. Her continual guidance and support while challenging me to achieve more is greatly appreciated.

I would also like to thank Richard Darlington, Paul Heerema, Kent Wheeler, and Dr. Michael Tait for their assistance and advice during the design and construction of the experimental program. Testing would not have been possible without their help.

My graduate school experience would not have been complete without the friendship of my fellow colleagues, including but not limited to Mike Kovacs, Taylor Steele, Saman Rastgoo Moghadam, and Farzad Nikfar.

Finally, I would like to gratefully acknowledge my fiancée, Carolyn van der Veen, for her unending support and patience. Her continual encouragement to put my best work forth was the driving force through much of this work.

TABLE OF CONTENTS

List of Figures	viii
List of Tables	ix
List of Symbols	x
Chapter 1: Introduction	1
1.1 Seismic Isolation	1
1.2 Column-Top Isolation	2
Chapter 2: Modelling of Elastomeric Bearings	6
2.1 Review of Existing Models	6
2.2 A Simple Stiffness Matrix Model	8
Chapter 3: Experimental Program	19
3.1 Outline	19
3.2 Test Specimens	20
3.3 Design of the Experimental Setup	23
3.4 Design of the Control System	27
3.5 Loading Protocol and Testing	29
3.6 Numerical Simulations	30
Chapter 4: Experimental and Numerical Results	32
4.1 Response of the Bearing	32
4.2 Response of the Column-Bearing Subassemblies	33
4.3 Post-Yield Response of a Column-Bearing Subassembly	47
Chapter 5: Performance as a Retrofit Strategy	49
5.1 Outline	49
5.2 Historical Structural Load Provisions	50
5.3 Building Design and Modelling	54
5.4 Ground Motion Selection and Scaling	58

5.5 Numerical Results	60
Chapter 6: Conclusions and Recommendations	70
6.1 Conclusions	70
6.2 Recommendations for Future Work	73
References	75
Appendix A: Source Code for the OpenSees Element	79
Appendix B: Coupon Testing Results	93
Appendix C: Supplementary Experimental Information	95

LIST OF FIGURES

1.1	Comparison of isolation retrofit techniques	2
2.1	Deformations of an infinitesimal rubber layer	10
2.2	Internal shear and moment of a deformed bearing	11
2.3	Deformation states for constructing a stiffness matrix	14
2.4	Degrees of freedom for the bearing stiffness matrix	18
3.1	A column-bearing subassembly in the test setup	19
3.2	Column-bearing connection for the subassemblies	21
3.3	Schematic of the experimental setup	23
3.4	Completed setup with the HSS64x64x4.8 subassembly installed	24
3.5	Control system diagram for the displacement-control scheme	27
3.6	Control system diagram for the load-control scheme	28
3.7	Cyclic displacement history	29
4.1	Response of the bearing under different cycling velocities	32
4.2	Experimental and model response of the bearing without a column	33
4.3	Comparison of the shear-displacement hystereses	34
4.4	Secant stiffness degradation of the bearing during each test	35
4.5	Experimental and model response of the bearing in the HSS127x127x8.0 subassembly	36
4.6	Experimental and model response of the bearing in the HSS102x102x8.0 subassembly	37
4.7	Experimental and model response of the bearing in the HSS76x76x4.8 subassembly	38
4.8	Experimental and model response of the bearing in the HSS64x64x4.8 subassembly	39
4.9	Experimental and model moment response at the bottom of the bearing in the HSS64x64x4.8 subassembly	39
4.10	Moment-displacement hystereses of each column	40
4.11	Moments and curvature cause by positive deformations	41

4.12	Bending moment diagrams at 20 mm displacement showing the progression of the inflection point with increasing column flexibility . . .	41
4.13	Components of the bearing shear and moment due to the bearing rotation only	43
4.14	Column displacement and column-bearing interface rotation relationship	44
4.15	Effect of the stiffness ratio on the peak column displacement ratio and base moment	45
4.16	Global shear-displacement hystereses of each subassembly	46
4.17	Post-yield response of the bearing in the HSS76x76x4.8 subassembly .	47
5.1	Structural layouts of the original and retrofit frames	49
5.2	Seismic zoning map in the 1965 National Building Code of Canada .	51
5.3	5% Damped response spectra of selected ground motions	60
5.4	Peak interstory drifts and floor accelerations during the DBE motions	61
5.5	Peak interstory drifts and floor accelerations during the MCE motions	61
5.6	Comparison of the pre- and post-retrofit moment-rotation hystereses for beams on each floor during the MCE Loma Prieta motion	62
5.7	Comparison of the peak moments in the first story columns	63
5.8	Peak elastic bending moment diagram in the original MRF during the DBE level Imperial Valley motion	64
5.9	Peak elastic bending moment diagram in the retrofit during the DBE level Imperial Valley motion	65
5.10	Response time history of a corner bearing during the MCE level Loma Prieta motion	66
5.11	Response time history of a center bearing during the MCE level Loma Prieta motion	67
5.12	5% Damped floor response spectra for the DBE level motions	68
5.13	5% Damped floor response spectra for the MCE level motions	69
B.1	Results from the HSS127x127x8.0 coupon testing	93
B.2	Results from the HSS102x102x8.0 coupon testing	94
B.3	Results from the HSS76x76x4.8 coupon testing	94
B.4	Results from the HSS64x64x4.8 coupon testing	94

LIST OF TABLES

3.1	Comparison of the bearing properties with the prototype	20
3.2	Column specimen properties	21
3.3	Strain gauge placement on each column	26
3.4	Tests conducted during the experimental program	30
5.1	Wind amplification factor for height segments	53
5.2	Selected frame sections	55
5.3	Bearing design values	57
5.4	Selected ground motions for nonlinear time history analyses	59
5.5	Peak bearing responses during the MCE level motions	68
C.1	Instrumentation channels	95
C.2	Commercial instrumentation and equipment used in the experimental setup	96

LIST OF SYMBOLS

A	Coefficient for the general solution to the differential equation
b	Strain hardening ratio
B	Coefficient for the general solution to the differential equation
$cR1$	Stress-strain shaping parameter
$cR2$	Stress-strain shaping parameter
$(EI)_c$	Column flexural stiffness
$(EI)_{\text{eff}}$	Effective bearing flexural stiffness
EI_s	Modified bearing flexural stiffness
G	Shear modulus of the bearing rubber
GA_s	Modified bearing shear stiffness
h	Total height of the bearing
I	Moment of inertia
k_b	Design lateral stiffness of the bearing
k_c	Lateral stiffness of the column
K	Bulk modulus of the bearing rubber
L	Column length
M_1	Moment at the bottom of the bearing
M_2	Moment at the top of the bearing
$M(x)$	Internal bending moment at a distance x from the bottom of the bearing
M_θ	Component of moment due to rotation
P	Axial load on the bearing
r	Radius of the bearing
$R0$	Stress-strain shaping parameter
S	Shape factor of the bearing
SR	Stiffness ratio between the bearing and the column
t	Thickness of an individual rubber layer
t_r	Total thickness of all rubber layers
t_s	Thickness of an individual steel shim
u_1	Lateral displacement at the bottom of the bearing

u_2	Lateral displacement at the top of the bearing
$u(x)$	Lateral displacement at a distance x from the bottom of the bearing
V_1	Shear at the bottom of the bearing
V_2	Shear at the top of the bearing
$V(x)$	Internal shear at a distance x from the bottom of the bearing
V_θ	Component of shear due to rotation
x	Current distance of a cross section from the bottom of the bearing
α	Simplifying factor
β	Simplifying factor
$\gamma(x)$	Shear strain at a distance x from the bottom of the bearing
Δ	Lateral displacement of the bearing
θ	Rotation at the column-bearing interface
λ	Simplifying factor
σ_y	Steel yield stress
ϕ_1	Rotation at the bottom of the bearing
ϕ_2	Rotation at the top of the bearing
$\phi(x)$	Rotation at a distance x from the bottom of the bearing

CHAPTER 1: INTRODUCTION

1.1 Seismic Isolation

Seismic isolation has been proven to significantly improve the structural performance of buildings as well as safeguarding building equipment and contents, which often have significant replacement costs [1]. Isolation is most commonly implemented by constructing a flexible layer between the ground and structure, decoupling the structure from ground motions, reducing both interstory drifts and floor accelerations. The flexible layer is traditionally bound by rigid diaphragms both above and below the layer to distribute shear forces and deform isolation bearings in pure translation, having no rotation of the endplates. To accommodate lateral movement of the building, excavation of a seismic gap is required around the structure.

Using isolation for seismic retrofit has been shown to be an effective strategy for improving the response of existing structures [2]. The benefits of isolation for the seismic rehabilitation of buildings is recognized by the Federal Emergency Management Agency (FEMA) and recommended as an effective strategy, particularly when enhanced performance is desired [3]. Numerous isolation retrofit projects have been completed using seismic isolation, examples of which include San Francisco City Hall, Tokyo Station, Long Beach Hospital, and the Hearst Mining Building on UC Berkeley campus [4, 5].

Despite the benefits that seismic isolation can offer, traditional installations can be expensive, especially in retrofit applications. For new construction, requiring rigid

diaphragms above and below the isolation layer and a seismic gap around the building can increase project costs. In addition to these costs, retrofit applications also require excavation underneath the building and extensive foundation work may be necessary, further exacerbating costs. As a result, isolation retrofit projects often have large project budgets, with the isolation bearings themselves only accounting for a small percentage of the total costs [4]. Due to high retrofit costs, applications of isolation retrofit are typically limited to buildings with historic or functional significance such as the previously mentioned projects.

1.2 Column-Top Isolation

To mitigate some of the major expenses associated with isolation and to extend isolation retrofit to a more general class of structures, bearings may be placed at the tops of columns [2], herein referred to as column-top isolation. In this configuration, an additional diaphragm and a seismic gap are no longer necessary, as depicted in Figure 1.1. In addition, column-top isolation may also potentially circumvent the need for excavation and foundation work in retrofit applications to further reduce costs.

While a traditional isolation system simplifies the behaviour of the bearings by maintaining parallel endplates, column-top isolation may not ensure that endplates remain parallel. In the case of retrofit applications, significant stiffening of the columns may

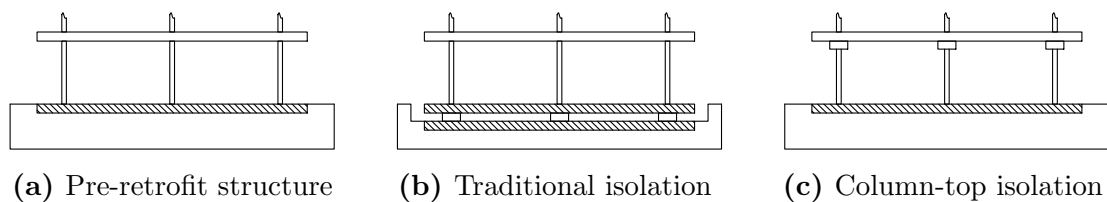


Figure 1.1: Comparison of isolation retrofit techniques

not be desirable either architecturally or economically. For new construction, supporting columns may also tend towards more compact and economical designs. As a result, columns beneath the isolation layer may not provide rigid boundary conditions for the bearings. This would lead to endplates rotating during displacement and would violate the assumption that endplates remain parallel made by the majority of bearing models. While there has been investigation into flexible end conditions for friction pendulum bearings [6, 7], for elastomeric bearings, work has mostly been limited to fixed end rotations [8, 9] which may arise from support settlement or sagging of structural elements.

Despite few studies on the behaviour of column-top isolation systems, a handful of new construction has recently adopted the strategy to reduce project costs. Examples of this include the Main Building of the Institute of Technology by the Shimizu Corporation, using lead rubber bearings on the tops of concrete columns [10]; the Christchurch Justice and Emergency Services Precinct, using lead rubber bearings and PTFE sliders on the tops of concrete columns [11]; and an extension to the Tipping Structural Engineers office, using triple friction pendulum bearings spliced into concrete filled steel tube columns [12]. In these applications, designers have used large, stiff supporting columns to minimize column displacements and provide near-rigid boundary conditions for isolators, avoiding issues concerning the effect of flexible end conditions. While this is sound practice for new construction, this may not always be economical or feasible as discussed previously.

The research presented in this work aims to investigate the effects of flexible columns connected to elastomeric isolation bearings and the performance of column-top isolation as a retrofit strategy. The investigation begins with a study on the analytical

modelling of elastomeric bearings subjected to flexible end conditions. Previous theoretical studies have shown that rotation of the bearing endplates can affect the lateral stiffness and stability of elastomeric bearings [8, 13, 14], but have focused on constant rotations or fixed-free configurations. To further the current state of research, a four degree of freedom stiffness matrix was developed to model the behaviour of elastomeric bearings, consisting of translation and rotation degrees of freedom at both endplates of the bearing. The model accounts for the effects of compressible rubber, P- Δ moments due to large isolator displacements, the effect of the axial load on the lateral stiffness, and the effect of endplate rotations on the lateral stiffness.

To validate the bearing model and investigate the column-bearing interaction in a column-top isolation system, an experimental program was conducted using four sub-assemblies consisting of a single column and elastomeric bearing. The test specimens used steel hollow structural sections for the columns with varying section sizes to provide a range of flexibilities and strength limits. The $1/4$ scale specimens were tested under quasi-static conditions with a cyclic lateral displacement history applied while a constant axial load was maintained on the subassemblies. Numerical simulations of the experimental setup were performed using the developed bearing model and results were compared with experimental findings.

Lastly, the performance of a column-top isolation system as a retrofit strategy was assessed through nonlinear time history analyses of a pre- and post- retrofit frame. The original moment resisting frame was designed according to the 1965 National Building Code of Canada [15] and was retrofitted with elastomeric bearings on the tops of the first story columns. Suites of ground motions at various hazard levels were selected and scaled to hazard levels prescribed in the 2010 National Building Code [16], and

comparisons between the two frames are made to determine the effectiveness of the retrofit strategy.

While this research focuses on the use of column-top isolation systems, the results may also find applications in scenarios where isolation bearings have flexible end conditions such as sub- or superstructure flexibility, isolation of bridge piers, isolation of tall buildings susceptible to rocking, and bearing connections to flexible diaphragms.

CHAPTER 2: MODELLING OF ELASTOMERIC BEARINGS

2.1 Review of Existing Models

When modelling the behaviour of elastomeric isolation bearings, the theory proposed by Haringx [17] is often used to form the basis of many studies. The theory was developed to quantify the buckling load of short rubber mountings used for vibration isolation by accounting for the large shear deformations expected with stalky rubber rods. The deformations of a rubber mounting are characterized by independent variables to express the lateral displacement and cross sectional rotation at any point along the height of the rod. The theory results in a differential equation requiring boundary conditions for the displacement and rotation at both ends of the mounting, and the resulting critical load can be determined from the solution. Gent [18] later studied the buckling load of multiple rubber blocks on top of one another with steel plates separating them by extending Haringx's theory. The grouping of the rubber and steel was treated as a homogenous material, and the buckling theory compared well with experimental results. The stability aspects of undisplaced elastomeric isolation bearings were studied in a similar manner by Derham and Thomas [19], Stanton et al. [20], and Kelly [4]. Koh and Kelly [21] and Tsai and Hsueh [22] used the premise of the theory to develop viscoelastic models characterizing the lateral behaviour of elastomeric bearings under dynamic loading and found good agreement with experimental results.

Although all of the studies cited above are extensions of the Haringx theory, each

makes a significant assumption concerning the boundary conditions of the bearing, namely, that endplates remain parallel. In traditional installations where the isolation bearings are bound by rigid diaphragms both above and below, the assumption that endplates remain parallel is valid. However, in some novel installations where bearings may be connected to flexible elements or in the case of support settlement, rotation of the bearing endplates can occur. Imbimbo and Kelly [13] considered the impact of endplate rotations on the undisplaced stability of elastomeric bearings by modifying the boundary conditions used in the solution to the differential equation derived by Haringx. The study concluded that the buckling load of a fixed-free configuration can be as little as half of the buckling load of an equivalent fixed-fixed configuration. Koh and Kelly [23] simplified the theory to provide a simple model to capture the lateral behaviour of elastomeric bearings, allowing rotations of the endplates and a moment resistance to rotation at one end of the bearing. Comparisons with experimental results showed reliable characterization of the lateral behaviour when endplates remain parallel; however, no tests were conducted with endplate rotations. Karbakhsh Ravari et al. [8] followed the derivation presented by Haringx but with rotations present at both bearing endplates. The study examined the displacements and internal forces along the bearing for various configurations of constant rotations when subjected to constant loading. The results showed the lateral stiffness can significantly increase or decrease depending on the direction of rotation relative to the direction of translation. Chang [14] imposed various boundary conditions to derive a stiffness matrix for an individual rubber layer to study bearings with varying layer properties. Each rubber layer used a rigid offset to account for the steel shims, and was described by translation and rotation degrees of freedom at the top and bottom of each rubber-steel layer. A stiffness matrix for the bearing was constructed from the stiffness matrices of each layer, and various configurations were examined under constant loadings. The study

showed the lateral stiffness significantly decreases when an endplate is free to rotate, and the lateral stiffness is also more sensitive to variations in the axial load.

To the author's knowledge, the present state of research on modelling of elastomeric bearings with rotating endplates has been limited to fixed or free rotations. In addition, existing studies have only considered the internal deformations and forces that develop, rather than the interaction with connecting elements. To investigate the effects of varying rotational flexibility on the response of elastomeric isolation bearings and the interaction with connecting elements, the following section will derive a simple stiffness matrix to model the lateral displacement and rotation of both endplates of a bearing.

2.2 A Simple Stiffness Matrix Model

The following model is introduced to develop a simple stiffness matrix to describe the behaviour of a circular elastomeric bearing with varying endplate rotations. The foundation of the model is based on Haringx's theory [17], such that the deformation of the bearing at any cross section x is described by two independent variables: the lateral displacement, $u(x)$, and the rotation, $\phi(x)$. In the derivation, the effects of large shear displacements expected with thin rubber layers and P- Δ moments due to large isolator displacements are accounted for. The solutions to the functions for the lateral displacement and rotation arrive as general solutions, and require boundary conditions to determine the particular solutions. Various sets of boundary conditions for different deformation states are imposed to determine the required shear and moment at both ends of the bearing to maintain equilibrium of the deformation state under consideration.

The derivation begins with the formulation provided by Haringx [17] to solve the functions describing the lateral displacement and rotation along the height of the bearing. Once these functions are obtained, the methodology proposed by Chang [14] is used to construct a stiffness matrix by imposing boundary conditions for particular deformations. However, for both procedures a simpler derivation than shown in the original texts is provided. While the derivation shown by Chang results in a very large stiffness matrix due to constructing the bearing stiffness matrix from the stiffness matrices of each individual rubber-steel layer, the following derivation assumes a homogeneous material to form a smaller four degree of freedom stiffness matrix. To account for the presence of the steel shims, the shear stiffness and flexural stiffness of the rubber are increased by a factor of h/t_r [4], where h is the total height of the bearing and t_r is the total thickness of all rubber layers. In addition, all previous models have assumed the rubber in the bearing to behave as an incompressible material which limits the application to rubbers with high bulk modulus to shear modulus ratios [24]. To account for compressibility, the flexural stiffness of a circular rubber pad derived using a pressure solution by Kelly and Konstantinidis [24] is used. The resulting effective flexural stiffness, $(EI)_{\text{eff}}$, was determined to be

$$(EI)_{\text{eff}} = 2GIS^2 \left(1 - \frac{3GS^2}{K} \right) \quad (2.1)$$

where G is the shear modulus of the rubber, I is the moment of inertia, S is the shape factor, and K is the bulk modulus of the rubber. Applying the effective shear and flexural stiffness to the case of a circular rubber bearing and accounting for the steel shims, the modified shear stiffness, GA_s , and modified flexural stiffness, EI_s ,

are given as

$$GA_s = \pi Gr^2 \left(\frac{h}{t_r} \right) \quad (2.2)$$

$$EI_s = \frac{\pi Gr^6}{8t^2} \left(1 - \frac{3Gr^2}{4Kt^2} \right) \left(\frac{h}{t_r} \right) \quad (2.3)$$

where r is the radius of the bearing and t is the thickness of an individual rubber layer.

Considering the deformation of an infinitesimally thin rubber layer, the total lateral deformation can be determined as the sum of the lateral deformation caused by the rotation and the shear strain of the layer. Figure 2.1 depicts of combination of these deformations by showing the changes in the location of the top node, located in the middle of the layer width. From the undeformed shape, the rotation of the layer, $\phi(x)$, causes a small lateral displacement and a small vertical displacement. Combining the layer rotation with the shear strain of the layer, $\gamma(x)$, the top node undergoes a larger lateral and vertical displacement. Using a first order approximation, the sum of these

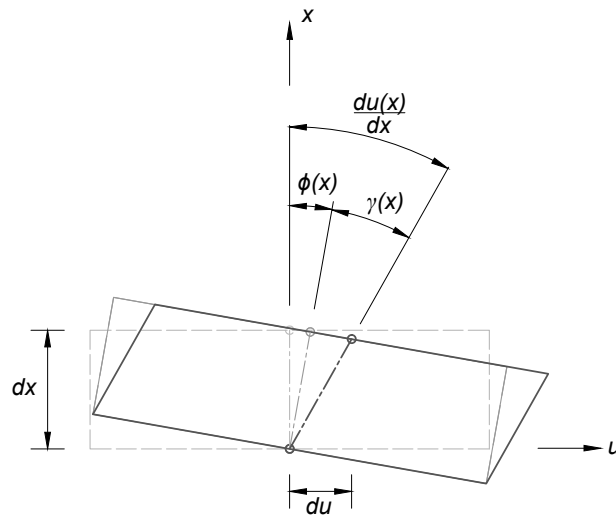


Figure 2.1: Deformations of an infinitesimal rubber layer

two behaviours is equal to the tangential lateral displacement across the layer [17]. Thus, the shear strain can be determined as

$$\gamma(x) = \frac{du(x)}{dx} - \phi(x) \quad (2.4)$$

and the shear force at a cross section a distance x from the bottom of the bearing can be expressed as a function dependent on the deformations at the cross section as

$$V(x) = GA_s \left(\frac{du(x)}{dx} - \phi(x) \right) \quad (2.5)$$

The bending moment at a cross section x can be expressed using the curvature equation from fundamental mechanics as

$$M(x) = EI_s \frac{d\phi(x)}{dx} \quad (2.6)$$

With the internal forces expressed as functions of the deformations, the equilibrium of a deformed bearing at a cross section x can be examined. Figure 2.2 shows the deformed shape of a bearing of height h , with the unknown forces required for equi-

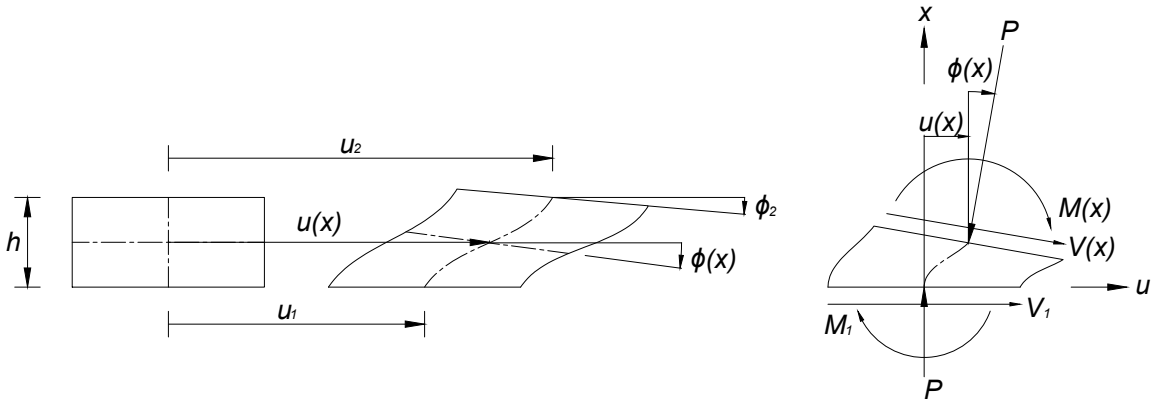


Figure 2.2: Internal shear and moment of a deformed bearing

librium. Note that the axial load, P , is applied to the normal of the rotated cross section. Taking the summation of forces in the horizontal direction, and the summation of moments about the center of the internal face to a first order approximation results in [4]

$$V_1 + V(x) - P\phi(x) = 0 \quad (2.7)$$

$$-M(x) - M_1 - Pu(x) + V_1x = 0 \quad (2.8)$$

Substituting the internal forces in Equations (2.5) and (2.6) into the equilibrium equations leads to

$$V_1 + GA_s \left(\frac{du(x)}{dx} - \phi(x) \right) - P\phi(x) = 0 \quad (2.9)$$

$$-EI_s \frac{d\phi(x)}{dx} - M_1 - Pu(x) + V_1x = 0 \quad (2.10)$$

To simplify the remainder of the derivation, it is useful to define two factors, α and β , such that

$$\alpha^2 = \frac{P(P + GA_s)}{EI_s GA_s} \quad (2.11)$$

$$\beta = \frac{GA_s}{P + GA_s} \quad (2.12)$$

Isolating for the rotation at any cross section x in Equation (2.9) results in

$$\phi(x) = \frac{V_1}{P + GA_s} + \beta \frac{du(x)}{dx} \quad (2.13)$$

Taking the derivative of Equation (2.13) with respect to x gives the relationship

$$\frac{d\phi(x)}{dx} = \beta \frac{d^2u(x)}{dx^2} \quad (2.14)$$

which can be substituted into Equation (2.10) and rearranged to obtain the differential equation

$$\frac{du^2(x)}{dx^2} + \alpha^2u(x) = \frac{\alpha^2V_1}{P}x - \frac{\alpha^2M_1}{P} \quad (2.15)$$

The general solution to the differential equation is of the form

$$u(x) = A \cos(\alpha x) + B \sin(\alpha x) + \frac{V_1}{P}x - \frac{M_1}{P} \quad (2.16)$$

where A and B are constant coefficients to be determined by boundary conditions.

Taking the derivative of the general solution with respect to x results in

$$\frac{du(x)}{dx} = \alpha B \cos(\alpha x) - \alpha A \sin(\alpha x) + \frac{V_1}{P} \quad (2.17)$$

and can be substituted into Equation (2.13) to obtain

$$\phi(x) = \alpha\beta B \cos(\alpha x) - \alpha\beta A \sin(\alpha x) + \frac{V_1}{P} \quad (2.18)$$

At this point, the Haringx theory [17] has been shown to obtain general solutions describing the lateral displacement, in Equation (2.16), and the rotation, in Equation (2.18), at any cross section x . The remainder of the derivation will follow the methodology proposed by Chang [14]; however, will focus on the deformations of the entire bearing rather than an individual rubber layer. The remaining unknowns in the general solutions are the coefficients A and B , and the shear force, V_1 , and moment, M_1 , at the bottom of the bearing. By imposing various boundary conditions to

describe a specific deformation state, these unknowns can be solved for and arranged to determine the required forces for equilibrium.

For the deformation state of pure translation, depicted in Figure 2.3 (a), the bottom of the bearing is fixed and a lateral displacement u_2 is applied at the top with zero rotation. The boundary conditions to satisfy this state are given as

$$\begin{aligned} u(h) &= u_2 & \phi(h) &= 0 \\ u(0) &= 0 & \phi(0) &= 0 \end{aligned}$$

Applying the lateral displacement and rotation boundary conditions at the bottom of the bearing leads to the solution of the coefficients as

$$A = \frac{M_1}{P} \quad (2.19)$$

$$B = -\frac{V_1}{\alpha\beta P} \quad (2.20)$$

Applying the rotation boundary condition at the top of the bearing and substituting the coefficients A and B , results in a relationship between the moment and shear at

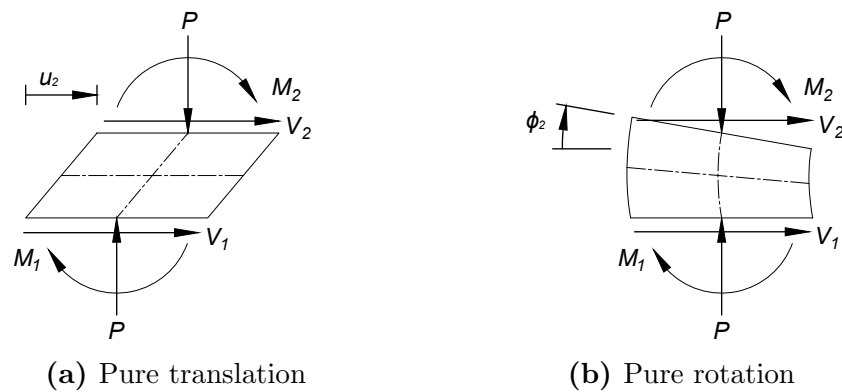


Figure 2.3: Deformation states for constructing a stiffness matrix

the bottom of the bearing as

$$\frac{M_1}{P} = \frac{V_1}{\alpha\beta P}\lambda \quad (2.21)$$

where λ is defined as

$$\lambda = \tan\left(\frac{\alpha h}{2}\right)$$

Applying the lateral displacement boundary condition at the top of the bearing and substituting the coefficients A and B , and the relationship in Equation (2.21), the shear force at the bottom of the bearing can be solved for. The resulting shear is a function of the lateral displacement, u_2 , and is given as

$$V_1 = - \left[\frac{\alpha\beta P}{2\lambda - \alpha\beta h} \right] u_2 \quad (2.22)$$

Substituting the shear at the bottom of the bearing into the relationship determined in Equation (2.21), the moment at the bottom of the bearing is found to be

$$M_1 = - \left[\frac{\lambda P}{2\lambda - \alpha\beta h} \right] u_2 \quad (2.23)$$

With the required shear and moment at the bottom of the bearing obtained, global equilibrium equations can be used to determine the shear, V_2 , and moment, M_2 , at the top of the bearing. These forces are found to be

$$V_2 = \left[\frac{\alpha\beta P}{2\lambda - \alpha\beta h} \right] u_2 \quad (2.24)$$

$$M_2 = - \left[\frac{\lambda P}{2\lambda - \alpha\beta h} \right] u_2 \quad (2.25)$$

With the solutions to the shear and moment at the top and bottom of the bearing

obtained, all of the required forces to maintain equilibrium of the deformation state are determined.

To consider the remaining deformation state, shown in Figure 2.3 (b), the bottom of the bearing is fixed and a rotation of ϕ_2 is applied to the top of the bearing with zero lateral displacement. From this deformation state a new set of boundary conditions arise to be used in the solution to the general equations given in Equations (2.16) and (2.18), and are given as

$$\begin{aligned} u(h) &= 0 & \phi(h) &= \phi_2 \\ u(0) &= 0 & \phi(0) &= 0 \end{aligned}$$

Note that the boundary conditions for lateral displacement and rotation at the bottom of the bearing are the same conditions used for the previous deformation state, and will yield the same coefficients determined in Equations (2.19) and (2.20).

Applying the lateral displacement boundary condition at the top of the bearing and substituting the coefficients A and B results in a relationship between the moment and shear at the bottom of the bearing as

$$\frac{M_1}{P} = \frac{V_1}{\alpha\beta P} \frac{\alpha\beta h - \sin(\alpha h)}{\lambda \sin(\alpha h)} \quad (2.26)$$

Applying the rotation boundary condition at the top of the bearing and substituting the coefficients A and B , and the relationship in Equation (2.26), the shear force at the bottom of the bearing can be solved for. The resulting shear is a function of the rotation at the top plate, ϕ_2 , and is given as

$$V_1 = \left[\frac{\lambda P}{2\lambda - \alpha\beta h} \right] \phi_2 \quad (2.27)$$

Substituting this shear into the relationship determined in Equation (2.26) results in the moment at the bottom of the bearing to be

$$M_1 = \left[\frac{P}{2\lambda - \alpha\beta h} \left(-\frac{1}{\alpha\beta} + \frac{h}{\sin(\alpha h)} \right) \right] \phi_2 \quad (2.28)$$

Using global equilibrium equations, the shear, V_2 , and moment, M_2 , at the top of the bearing are found to be

$$V_2 = - \left[\frac{\lambda P}{2\lambda - \alpha\beta h} \right] \phi_2 \quad (2.29)$$

$$M_2 = \left[\frac{P}{2\lambda - \alpha\beta h} \left(\frac{1}{\alpha\beta} - \frac{h}{\tan(\alpha h)} \right) \right] \phi_2 \quad (2.30)$$

With the required equilibrium forces for the two deformation states derived, a stiffness matrix can be constructed by considering the deformation states in various orientations. The resulting stiffness matrix is given as

$$\begin{bmatrix} V_1 \\ M_1 \\ V_2 \\ M_2 \end{bmatrix} = \frac{P}{2\lambda - \alpha\beta h} \begin{bmatrix} \alpha\beta & \lambda & -\alpha\beta & \lambda \\ \lambda & \frac{1}{\alpha\beta} - \frac{h}{\tan(\alpha h)} & -\lambda & -\frac{1}{\alpha\beta} + \frac{h}{\sin(\alpha h)} \\ -\alpha\beta & -\lambda & \alpha\beta & -\lambda \\ \lambda & -\frac{1}{\alpha\beta} + \frac{h}{\sin(\alpha h)} & -\lambda & \frac{1}{\alpha\beta} - \frac{h}{\tan(\alpha h)} \end{bmatrix} \begin{bmatrix} u_1 \\ \phi_1 \\ u_2 \\ \phi_2 \end{bmatrix} \quad (2.31)$$

Note that this is the same matrix determined by Chang [14] with the exception that this matrix represents an entire bearing of height h , rather than an individual rubber layer of thickness t . To align with the typical coordinates used by most software, the

matrix can be rewritten as

$$\begin{bmatrix} V_1 \\ M_1 \\ V_2 \\ M_2 \end{bmatrix} = \frac{P}{2\lambda - \alpha\beta h} \begin{bmatrix} \alpha\beta & -\lambda & -\alpha\beta & -\lambda \\ -\lambda & \frac{1}{\alpha\beta} - \frac{h}{\tan(\alpha h)} & \lambda & -\frac{1}{\alpha\beta} + \frac{h}{\sin(\alpha h)} \\ -\alpha\beta & \lambda & \alpha\beta & \lambda \\ -\lambda & -\frac{1}{\alpha\beta} + \frac{h}{\sin(\alpha h)} & \lambda & \frac{1}{\alpha\beta} - \frac{h}{\tan(\alpha h)} \end{bmatrix} \begin{bmatrix} u_1 \\ \phi_1 \\ u_2 \\ \phi_2 \end{bmatrix} \quad (2.32)$$

to correspond with the degrees of freedom indicated in Figure 2.4.

The resulting stiffness matrix was adapted into a new element for use with the Open System for Earthquake Engineering Simulation (OpenSees) [25]. The source code for the element can be viewed in Appendix A. The required parameters to construct the element are the bearing radius, the thickness of an individual rubber layer, the total thickness of all rubber layers, the total height of the bearing, the shear modulus of the rubber, and the axial load. The bulk modulus of the rubber can be included optionally to account for compressible effects.

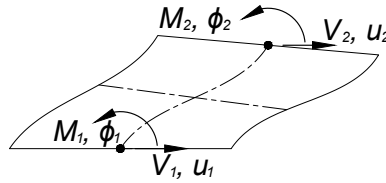
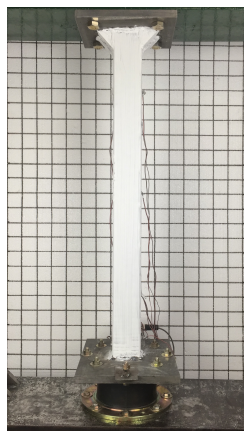
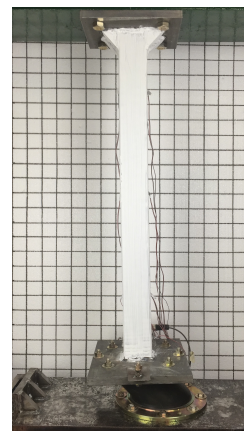


Figure 2.4: Degrees of freedom for the bearing stiffness matrix

CHAPTER 3: EXPERIMENTAL PROGRAM

3.1 Outline

To investigate the behaviour of a column-top isolation system with substructure flexibility, an experimental program was developed for testing at the Applied Dynamics Laboratory at McMaster University. Four subassemblies consisting of a single elastomeric bearing connected directly to a steel column, pictured in Figure 3.1, were studied under quasi-static cyclic testing with increasing amplitude. The specimens for the program were selected to be $1/4$ scale in an effort to reduce the loading requirements to magnitudes achievable with equipment available in the laboratory. To provide the necessary loading and displacement demands, an experimental setup was designed and constructed to apply a constant axial load on specimens while a cyclic lateral displacement was applied.

**(a)** Undeformed**(b)** Deformed**Figure 3.1:** A column-bearing subassembly in the test setup

The remaining sections of this chapter present the details associated with each aspect of the experimental program. This includes selection and detailing of the column-bearing specimens, design of the experimental setup, instrumentation, design of the control system, loading protocol, and testing. Lastly, numerical simulations of the experimental setup to be compared with experimental results are discussed.

3.2 Test Specimens

A typical circular elastomeric isolation bearing, manufactured to adhere to the scaling requirements, was procured for the experimental program. The details of the scaled bearing are presented in Table 3.1, and are compared with the prototype bearing. One isolation bearing was used for all tests conducted in the experimental program, and therefore non-permanent and removable connections were required. The bottom endplate of the bearing was secured to the experimental setup via bolted connection, while the opposite endplate was bolted to a plate section welded to the column end. Details of the column-bearing connection can be viewed in Figure 3.2.

Four steel columns made from square Hollow Structural Sections (HSS) were selected

Table 3.1: Comparison of the bearing properties with the prototype

Property	Prototype	¹ / ₄ Model
Radius, r (mm)	320	80
Area, A (mm ²)	321700	20110
Rubber layer thickness, t (mm)	7.92	1.98
Steel shim thickness, t_s (mm)	4.00	1.00
Total rubber thickness, t_r (mm)	158.4	39.7
Height, h (mm)	407.2	101.8
Shape factor, S	20.2	20.2
Shear modulus at 100%, G (MPa)	0.4	0.4
Bulk modulus, K (MPa)	1200	1200

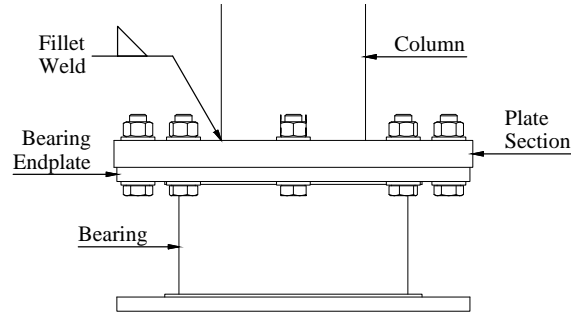


Figure 3.2: Column-bearing connection for the subassemblies

with varying section sizes to provide a range of substructure flexibility. All columns were 875 mm in length (3.5 m for the prototype) and are detailed in Table 3.2 with the respective depth-to-length ratio, moment of inertia, I , and yield strength, σ_y . Also included in Table 3.2 is a stiffness ratio, SR , defined as the ratio of the bearing lateral stiffness to the column lateral stiffness, and is determined by

$$SR = \frac{k_b}{k_c} = \frac{GA/t_r}{3(EI)_c/L^3} \quad (3.1)$$

where GA is the bearing shear stiffness, $(EI)_c$ is the flexural stiffness of the column, and L is the length of the column. The ratio is useful when investigating the effects of the substructure flexibility by using the relative stiffness of the subassembly, with a ratio of zero representing a rigid substructure. It should be noted that the lateral stiffness of the column is determined assuming a fixed-free structure as a result of the experimental findings discussed further on page 42.

Table 3.2: Column specimen properties

Column	Depth-to-Length (%)	I (10^6mm^4)	σ_y (MPa)	SR (%)
HSS127x127x8.0	14.5	7.73	380	2.93
HSS102x102x8.0	11.6	3.72	390	6.10
HSS76x76x4.8	8.71	1.00	384	22.7
HSS64x64x4.8	7.26	0.553	394	41.0

Tensile testing of coupons from each column was performed to determine the yield strength and behaviour of the steel. The results of the tensile testing can be found in Appendix B, along with comparisons to numerical modelling discussed further in section 3.6. An appropriate section size was estimated by assuming a rigid column and using basic structural mechanics with the design lateral stiffness of the bearing and the peak displacement demand to be imposed. With an estimated section as a reference, various smaller sections were analyzed through numerical simulations, discussed further in section 3.6, to select appropriate columns based on the analyses and availability for procurement. The largest section size was selected to provide near-rigid conditions for the substructure and no yielding behaviour, while the next smaller section was used to provide a more flexible substructure while still remaining elastic. The two most flexible columns were selected to provide highly flexible substructures and showed formation of a plastic hinge in the analyses. Yielding of the column in the experimental program was desirable in order to verify the ability of the numerical simulations to capture this behaviour. In practice, yielding of the substructure would be an undesirable characteristic and must be prevented to avoid concerns of soft story collapse mechanisms.

Columns were outfitted with plate sections welded to both ends. A plate at one end of the column was drilled to match the bolt hole pattern in the isolation bearing endplate, while the plate on the opposite end of the column was drilled to match a bolt hole pattern on the experimental setup. The bolted connections allowed for easily removing and replacing new columns for testing during the program. It was found that the weld strength of the column to plate connection farthest from the bearing would not provide adequate moment resistance, so these connections were reinforced with angled stiffeners welded between the column and plate.

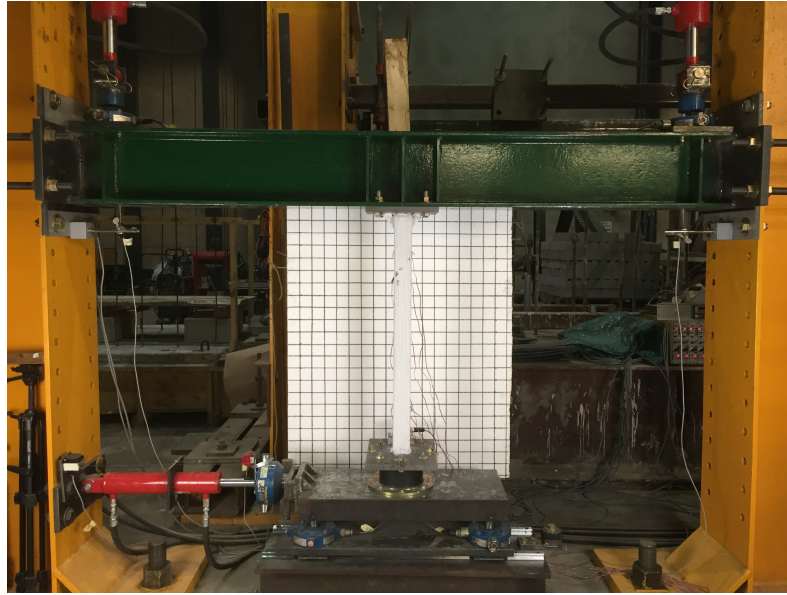


Figure 3.4: Completed setup with the HSS64x64x4.8 subassembly installed

support. The free ends of the threaded rods were also bolted to similar plates on the opposite sides of the reaction columns. To allow vertical movement of the loading beam, a polyoxymethylene layer, a synthetic polymer with a low friction coefficient and a high stiffness, was placed between the plate sections and polished steel plates bolted to the reaction columns to create a sliding surface. This configuration allowed the loading beam to move vertically with minimal force while supporting the lateral forces in the beam through bearing against the reaction columns. In addition, the distance between the loading beam and uniaxial table could be easily adjusted by raising or lowering the loading beam, vertical actuators, and sliding surfaces to the required height.

At the base of the setup, a uniaxial table was constructed on two linear sliders, and was driven by a horizontal actuator pin-connected to a reaction column. The table was able to reach a stroke length of ± 120 mm from the center position. Two sliding blocks were used with each linear rail and each connected to a plate at the base of

the table. Load cells connected to the plate, directly above each sliding block, were used to support a large plate where the isolation bearing would connect.

In total, four load cells were located underneath the plate supporting the isolation bearing, two load cells being on the East side of the plate and two on the West side separated at a distance of 622 mm. The measurements from the load cells were used to determine the moment reaction at the bottom of the bearing. Load cells were also placed in line with each actuator, with additional instrumentation to determine the displacement of the actuator. For the vertical actuators, linear variable displacement transducers (LVDTs) were located directly beneath the loading beam from where the actuator connected, and the horizontal actuator used a string pot (SP) to determine the displacement of the uniaxial table. An additional string pot was installed on the reaction column and connected to the column-bearing interface in order to determine the lateral displacement of the column only. With the measurements from the two string pots, the displacement the column could be subtracted from the total displacement of the uniaxial table to determine the lateral displacement of the isolation bearing. To measure the rotation of the column-bearing interface, an inclinometer (INCL) was affixed at the rear of the column-bearing connection. The locations of all the instrumentation used are also depicted in the schematic in Figure 3.3.

Lastly, each column specimen was outfitted with sets of strain gauges along the length. Each set consisted of two strain gauges located on opposite sides of the column to determine the internal bending moments, and the locations of each set are summarized in Table 3.3. Bending moments were expected to be largest at the top of the column where the subassembly connected to the loading beam, and placement of the first set of strain gauges was strategic to capture the formation of a plastic hinge if yielding

Table 3.3: Strain gauge placement on each column

Column	Location of strain gauge set from top of column (mm)				
	Set 1	Set 2	Set 3	Set 4	Set 5
HSS127x127x8.0	165.0	200.0	400.0	675.0	855.0
HSS102x102x8.0	134.6	200.0	400.0	675.0	855.0
HSS76x76x4.8	119.3	200.0	400.0	675.0	855.0
HSS64x64x4.8	104.1	200.0	400.0	675.0	855.0

occurred. Brescia et al. [26] studied the cyclic behaviour of steel HSS members and found the formation of a plastic hinge typically occurred a distance of 1.2 times the flange width away from the connection. The results from the study were used to determine the placement for the first set of strain gauges, while the remaining sets were placed along the column to determine the bending moment diagram.

Measurements were recorded from all instrumentation using a data acquisition system separate from the control system. As some instrumentation was used for both the control system and for measurements, the signals from these instruments were split using isolation circuits. The signals required isolation from each other so that when a sample was taken, the control system was not affected due to the electrical load the sampling would induce on the circuit. A sample rate of 10 Hz was used to capture the measurements; however, as a relay-style acquisition system was used, the actual sample rate during testing was 0.84 Hz due to the number of channels being sampled. A complete list of all instrumentation channels can be found in Appendix C, along with additional information regarding instrumentation and equipment used in the experimental setup.

3.4 Design of the Control System

Control of the experimental setup to apply the appropriate loading and displacement history required two control schemes. In both schemes, the horizontal actuator driving the uniaxial table and the vertical actuator on the East side of the setup were under a displacement-control mode; however, the vertical actuator on the West side of the setup required both displacement-control and load-control modes. All actuators in the setup used proportional-integral (PI) controllers regardless of the control mode. The East vertical actuator was used to maintain a horizontal loading beam by using the difference in displacement between the two vertical actuators as feedback, and attempted to maintain this difference at zero.

A displacement-control mode was required for positioning of the loading beam when installing the specimens into the setup and for the initial loading stage during test-

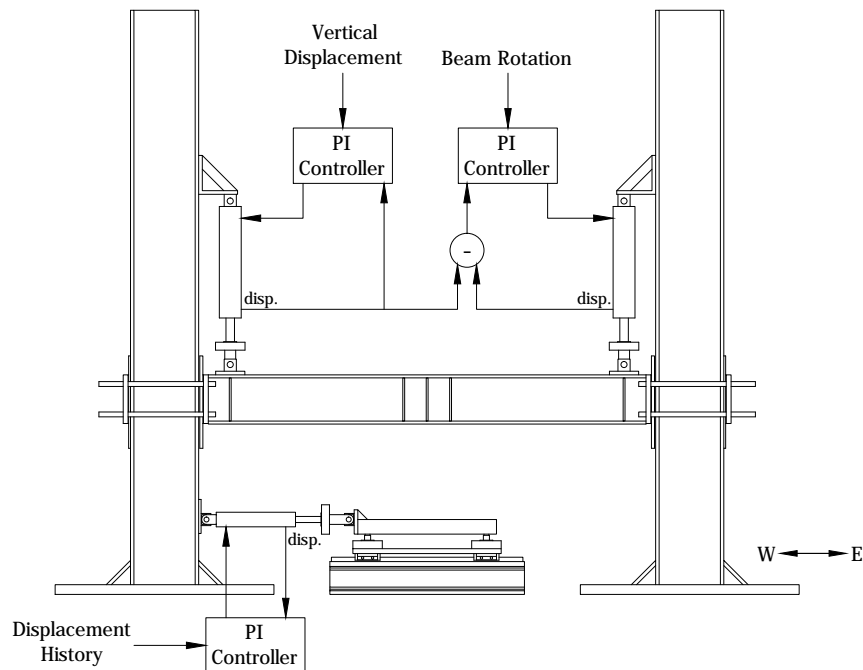


Figure 3.5: Control system diagram for the displacement-control scheme

ing. The control system scheme for this mode, shown in Figure 3.5, used a typical configuration with the displacement of the actuator itself as the feedback signal. A load-control mode was required during testing to maintain a constant axial load regardless of any vertical displacements that the test specimens may undergo. Under this mode, shown in Figure 3.6, the summation of the two loads from each vertical actuator was used for feedback to the controller to indicate the total axial load on the specimen.

As a result of two separate control systems acting on the loading beam, the response of one system may elicit a response in the other, in-turn causing a response in the first system again and create a cyclic teetering of the loading beam. In order to avoid this effect, tuning of the two PI controllers was performed to minimize persistent teetering. The controller ensuring the loading beam remained horizontal was given priority by using a higher proportional gain, while the controller determining the vertical position

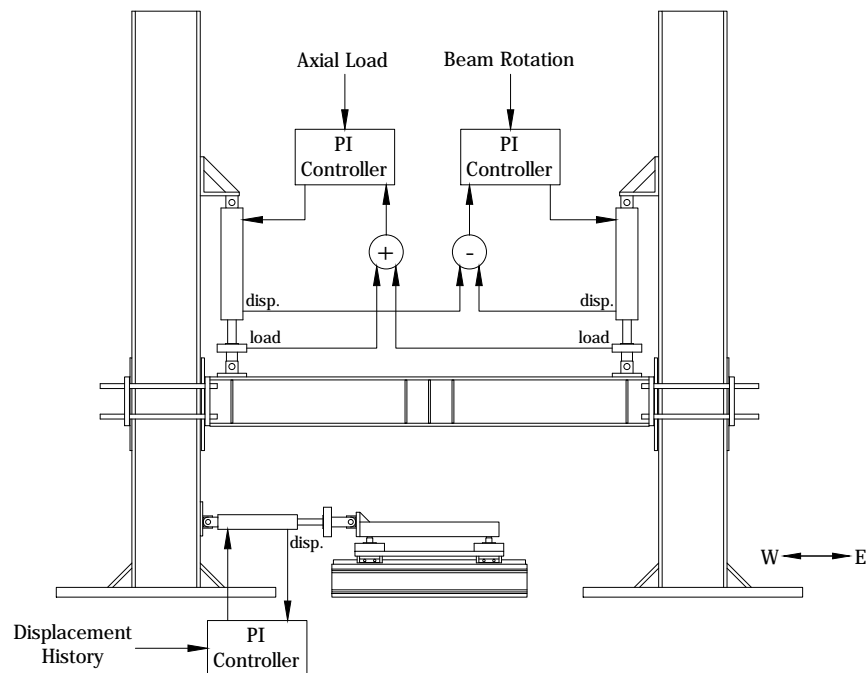


Figure 3.6: Control system diagram for the load-control scheme

was given a lower proportional gain. This caused the system to respond quickly to differences in height between the two actuators, and slower to the vertical position of the beam, reducing any cyclic responses between the two systems.

3.5 Loading Protocol and Testing

Once a test specimen was installed in the setup, a loading protocol began to lower the loading beam in the displacement-control scheme until a small compressive axial load of 5 kN was reached. The system then automatically switched into the load-control scheme to ramp the axial load to 120.6 kN (6 MPa of pad pressure on the bearing), and maintained the load for the duration of the test. A quasi-static cyclic displacement history was supplied to the horizontal actuator driving the uniaxial table at a constant velocity of 1 mm/s. The displacement history, shown in Figure 3.7, consisted of multiple cycles at ± 10 mm, ± 20 mm, ± 40 mm, ± 60 mm, ± 80 mm, and ± 100 mm. Each specimen underwent the same loading protocol with the exception of the HSS64x64x4.8 subassembly, which was stopped at the completion of the ± 80 mm cycles due to excessive rotations at the column-bearing interface and a negative tangential lateral stiffness of the subassembly.

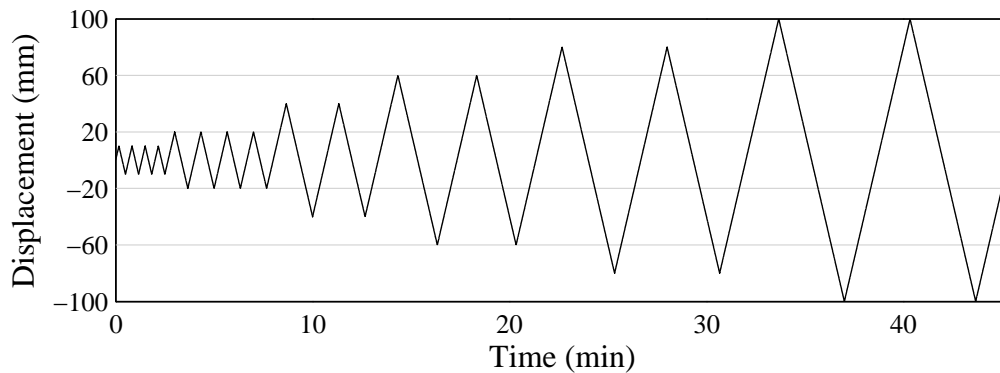


Figure 3.7: Cyclic displacement history

Table 3.4: Tests conducted during the experimental program

Date	Specimen	Notes
Nov. 26, 2015	Bearing only	Cycling velocity of 2 mm/s
Dec. 2, 2015	Bearing only	Cycling velocity of 1 mm/s
Jan. 5, 2016	HSS127x127x8.0 subassembly	Standard test
Jan. 6, 2016	HSS102x102x8.0 subassembly	Standard test
Jan. 13, 2016	HSS76x76x4.8 subassembly	Standard test
Jan. 13, 2016	HSS76x76x4.8 subassembly	Post-yield test
Jan. 25, 2016	HSS64x64x4.8 subassembly	Standard test, stopped early

A record of all tests conducted during the experimental program are listed in Table 3.4. Initial testing was performed on the elastomeric bearing only by lowering the loading beam and connecting the bearing directly to the beam and the uniaxial table. Full tests of the bearing were conducted at constant cycling velocities of 2 mm/s and 1 mm/s to compare results and ensure results were rate-independent. The loading beam was then raised to accommodate the column-bearing subassemblies, and standard testing was conducted for each specimen. The post-yielding behaviour of a subassembly was investigated by retesting the HSS76x76x4.8 subassembly and comparing the results with the initial testing.

3.6 Numerical Simulations

Modelling of the experimental setup was conducted in OpenSees [25] using the newly created bearing element derived in section 2.2. The HSS127x127x8.0 and HSS102x102x8.0 columns were modelled with elastic Timoshenko beam column elements to account for the shear deformations expected with the large depth-to-length ratios of these columns. In addition, these columns were expected to remain elastic during testing. The remaining columns, having negligible depth-to-length ratios and were expected to yield, were modelled with nonlinear beam column elements con-

structed with fiber sections. Elastic beam column elements were used to model the loading beam and reaction frames in the experimental setup. Although the deformations in these members were expected to be small, the elements were included in the numerical simulations to help improve accuracy. The stress-strain response of the steel columns was modelled by a Giuffr -Menegotto-Pinto model calibrated to experimental results from coupon testing from each column. Results of the coupon testing with comparisons to the numerical calibrations can be found in Appendix B. Simulations of the experimental setup followed the same loading protocol described previously for the experimental testing.

CHAPTER 4: EXPERIMENTAL AND NUMERICAL RESULTS

4.1 Response of the Bearing

Initial testing conducted on the bearing without a column was used to find the baseline behaviour of the elastomeric bearing and ensure there was no sensitivity to strain rate around the low-velocities used in the testing. For these initial tests the endplates were kept parallel to represent the typical behaviour of elastomeric bearings. Preliminary testing using the full cyclic displacement history was conducted first at a constant velocity of 2 mm/s and then 1 mm/s, and comparisons of the results are shown in Figure 4.1. The figure presents the shear-displacement and moment-displacement hystereses, where the moment is the reaction measured at the top of the bearing. In both hystereses, the comparison indicates the cycling velocity is slow enough to provide negligible differences in the results. Testing of the bearing at 2 mm/s provided slightly higher hardening of the lateral stiffness at extreme shear strains; however, this is likely associated with scragging of the elastomer as this was the first tests to exert

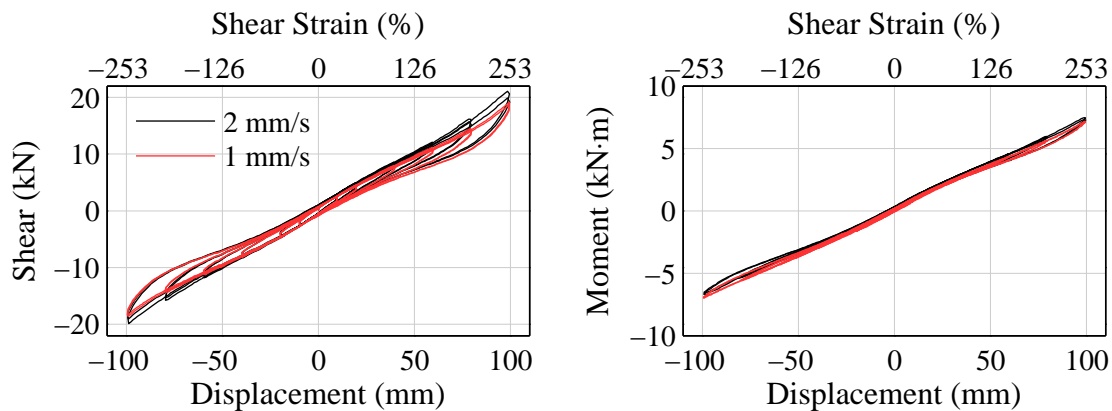


Figure 4.1: Response of the bearing under different cycling velocities

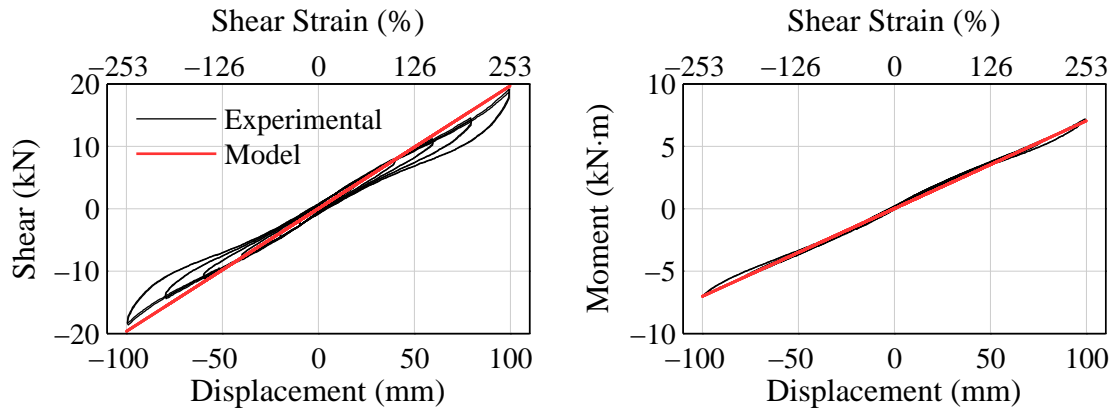


Figure 4.2: Experimental and model response of the bearing without a column

large shear strains on the bearing. The results of this preliminary testing indicate experimental results are not sensitive to the low velocities used, and the remainder of the test program was conducted at a 1 mm/s so that more detailed data could be sampled during the testing.

The results obtained from testing of the bearing at a cycling velocity of 1 mm/s were also used to assess the accuracy of the analytical model. Figure 4.2 compares the experimental and modelling results for the shear-displacement and moment-displacement hystereses, and shows good accuracy of the model when endplates remain parallel. The model provides a reliable approximation for the secant stiffness of the bearing and an accurate representation of the linear bending moments developed, indicating reliable terms in the stiffness matrix in Equation (2.32) for the shear-displacement and moment-displacement relationships.

4.2 Response of the Column-Bearing Subassemblies

The effect of varying the column stiffness on the shear-displacement hystereses for the subassembly is presented in Figure 4.3 (a), comparing the results from the

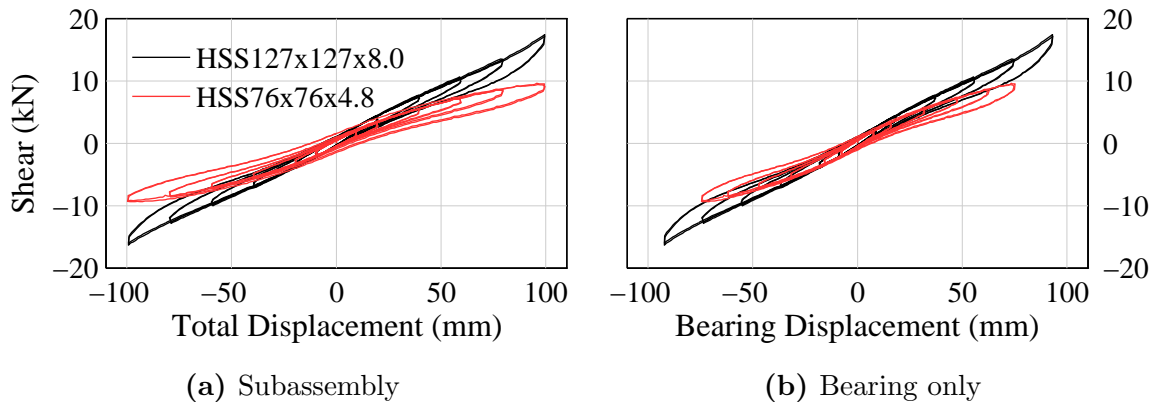


Figure 4.3: Comparison of the shear-displacement hysteresses

HSS127x127x8.0 and HSS76x76x4.8 columns. As more flexible columns were installed, the stiffness of the subassembly decreased as expected; however, the decrease was not solely due to the increased column flexibility. The bearing also exhibited a decrease in stiffness as seen in the shear-displacement hysteresis of the bearing in Figure 4.3 (b), determined by subtracting the column displacement from the total displacement. As more flexible columns were tested in the subassembly, the bearing had more flexible end conditions and experienced larger endplate rotations, with peak values of 0.010 rad, 0.014 rad, 0.031 rad, and 0.044 rad for each increasingly flexible column. The impact of the endplate rotations resulted in a reduction in lateral stiffness of the bearing and confirms previously theoretical studies [8, 13, 14].

The secant stiffness of the bearing at the maximum displacement of each cycle was determined for each test and is plotted in Figure 4.4. Testing of the bearing only, without a column, gives the baseline behaviour of the isolation bearing with parallel endplates. For this condition, the bearing experienced a decrease in stiffness after small displacements and light hardening behaviour at shear strains above 200%, as is typical for natural rubber [27]. The presence of flexible columns resulted in decreased bearing stiffness, the effect of which is magnified with larger displacements. For ex-

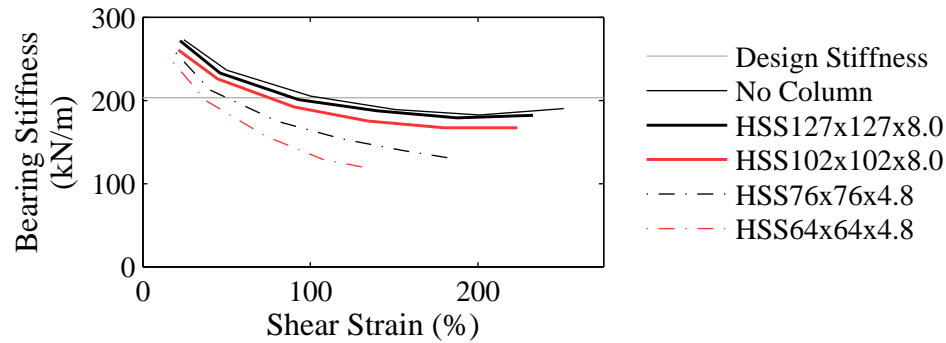


Figure 4.4: Secant stiffness degradation of the bearing during each test

ample, the most flexible column reduced the bearing stiffness to 58% of the design stiffness at a shear strain of 100%. Thus, the impact of flexible end conditions on an isolation bearing can significantly alter the lateral stiffness and must be considered in order to estimate the isolation period and peak displacement with reasonable accuracy.

More flexible columns also resulted in lower displacements in the isolation bearing due to increased displacements in the column. This can be seen by comparing the hysteresis loops in Figure 4.3 (b), where the bearing displacement in the HSS76x76x4.8 subassembly is notably lower than the bearing displacement in the HSS127x127x8.0 subassembly. The effect can also be observed in Figure 4.4, where subsequent tests with more flexible columns result in lower shear strains in the bearing at each displacement cycle.

The HSS127x127x8.0 column provided a very stiff end condition for the isolation bearing. Rotations at the column-bearing interface were small (0.010 rad maximum) and had little impact on the lateral stiffness of the bearing. Due to the high stiffness of the column, the displacement demands were largely concentrated in the bearing with small displacements measured in the column. The high moment resistance and small

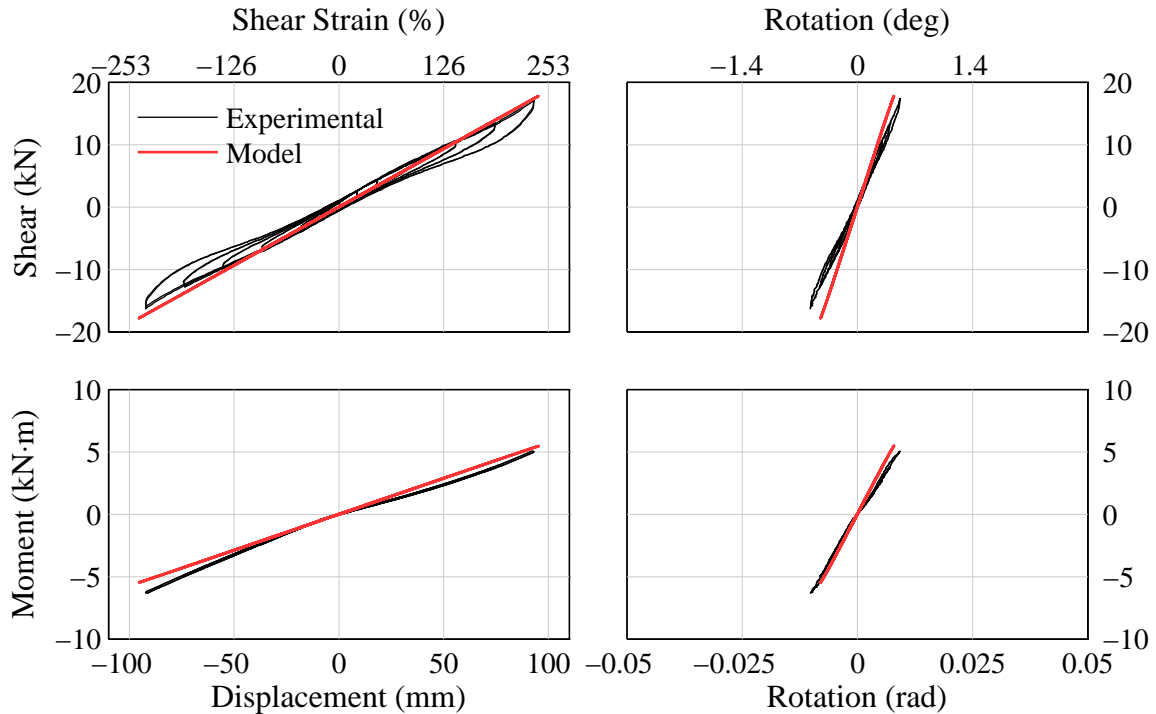


Figure 4.5: Experimental and model response of the bearing in the HSS127x127x8.0 subassembly

displacement demands on the column resulted in the column remaining in the elastic range during testing. The behaviour of the bearing within the subassembly is shown in Figure 4.5 with comparisons to the modelling. Note that the moment referred to in the figure is the moment that developed at the column-bearing interface. The bearing exhibited nearly linear responses in the shear-displacement, shear-rotation, moment-displacement, and moment-rotation relationships. The model was found to be reliable for most relationships but underestimated the amount of rotation at the column-bearing interface.

The HSS102x102x8.0 column showed a similar elastic behaviour but with larger displacements in the column and larger rotations at the column-bearing interface. The bearing response in Figure 4.6 shows similar results to the bearing response in the

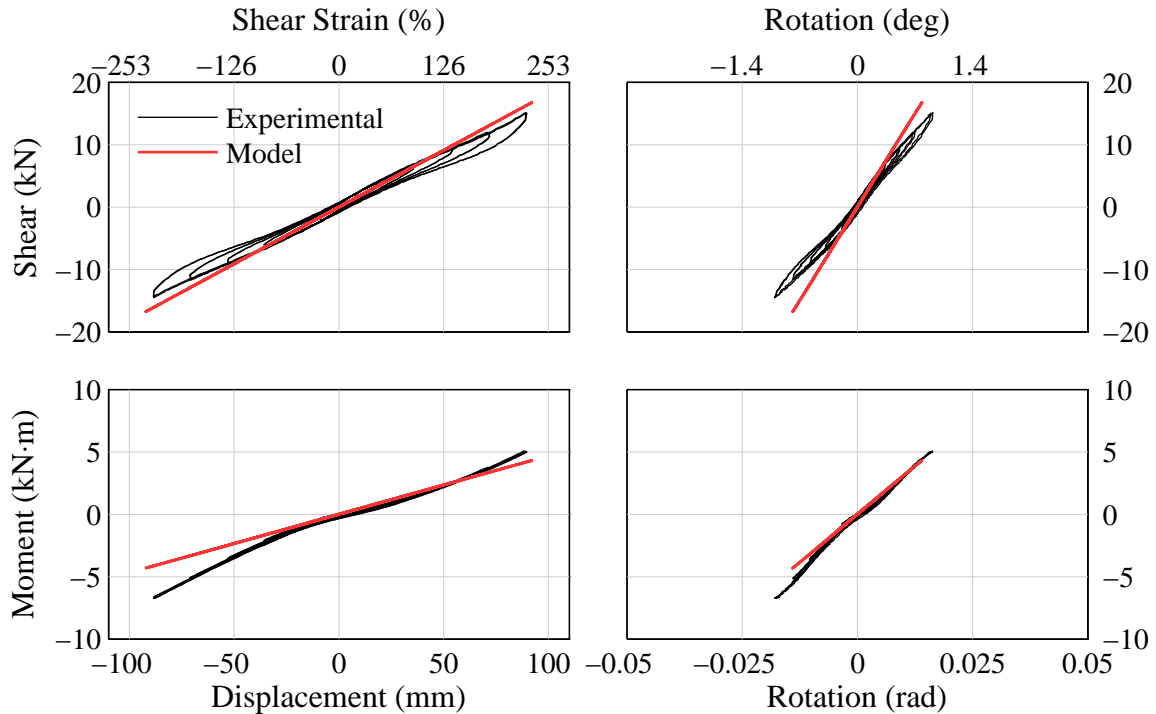


Figure 4.6: Experimental and model response of the bearing in the HSS102x1027x8.0 subassembly

HSS127x127x8.0 subassembly; however, the bending moment began to exhibit a nonlinear response at $\pm 60\%$ shear strain. This effect is significantly more pronounced with the HSS76x76x4.8 column, shown in Figure 4.7, where the nonlinear behavior also began at a shear strain of $\pm 60\%$. The stiffness degradation described earlier was more significant in the bearing response from the HSS76x76x4.8 subassembly and can be seen in the shear-displacement hysteresis of Figure 4.7. The shear-rotation response also began to show nonlinear behaviour, with rotations exceeding those predicted by the modelling.

The results of the HSS64x64x4.8 subassembly are shown in Figure 4.8, and continue the progressions observed in the previous subassemblies. The bearing experienced lower displacement demands due to a higher distribution of displacements to the

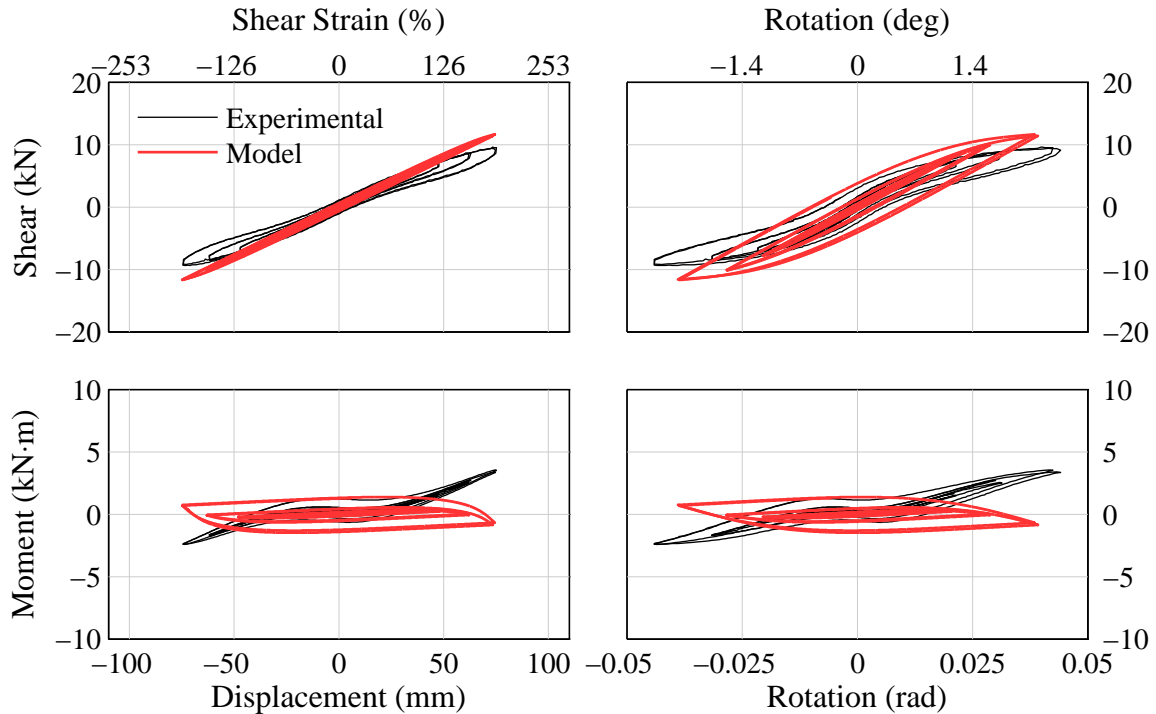


Figure 4.7: Experimental and model response of the bearing in the HSS76x76x4.8 sub-assembly

column and slight yielding occurred at the column end farthest from the bearing. Large rotations at the column-bearing interface were observed at peak displacements and are shown experimentally in Figure 4.11 (c). The bearing continued to exhibit and amplify the nonlinear behaviour in the bending moment as shear strains exceeded $\pm 60\%$. Considering the bearing response in all tests, the model is shown to be reliable when endplates remain parallel, and for rotated conditions up to shear strains of $\pm 60\%$. However, even in this range, the model underestimates the amount of rotation at the column-bearing interface.

Comparing the experimental and model responses of the moment at the bottom of the bearing (opposite to the column) had similar findings as the moment at the top of the bearing. As an example, Figure 4.9 presents the moment response at the bottom of

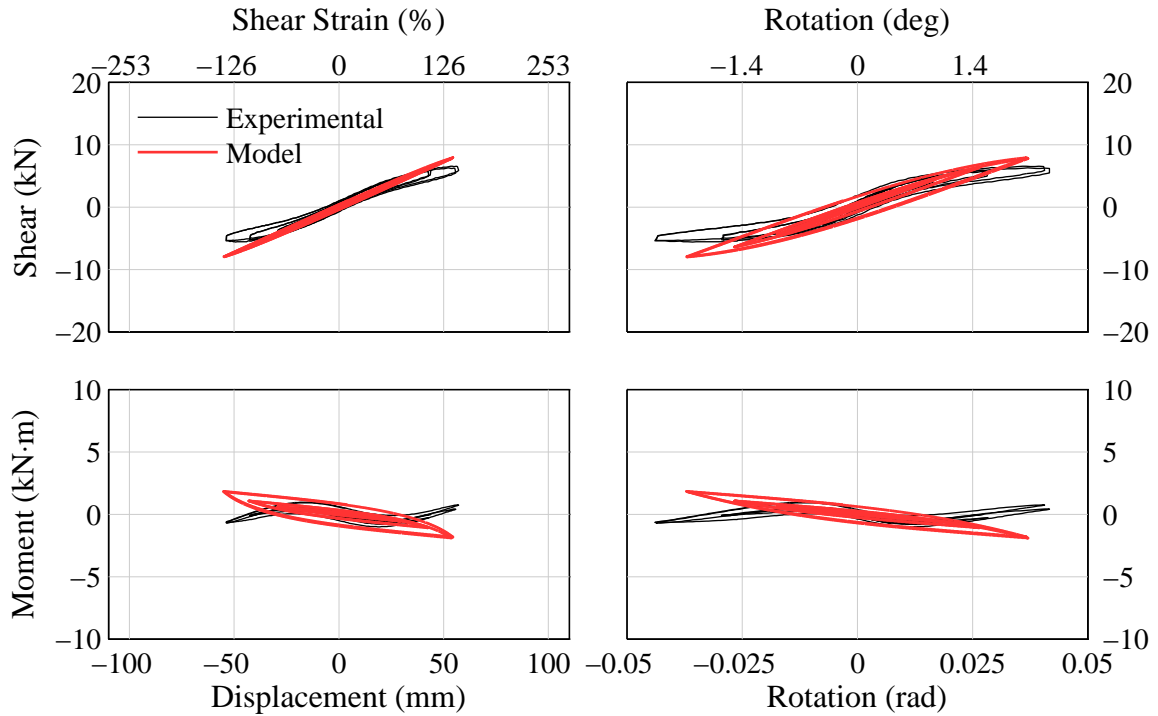


Figure 4.8: Experimental and model response of the bearing in the HSS64x64x4.8 sub-assembly

the bearing for the HSS64x64x4.8 subassembly, showing a similar nonlinear response noted previously at a shear strain of $\pm 60\%$.

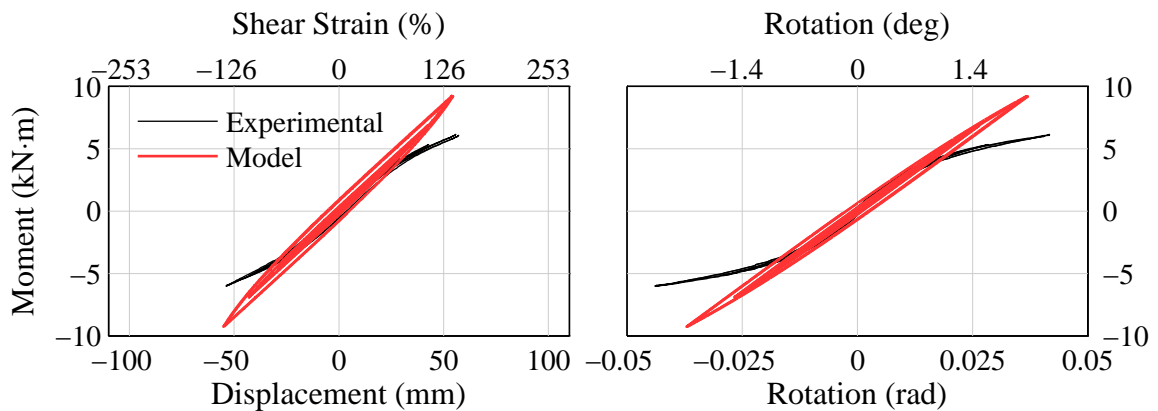


Figure 4.9: Experimental and model moment response at the bottom of the bearing in the HSS64x64x4.8 subassembly

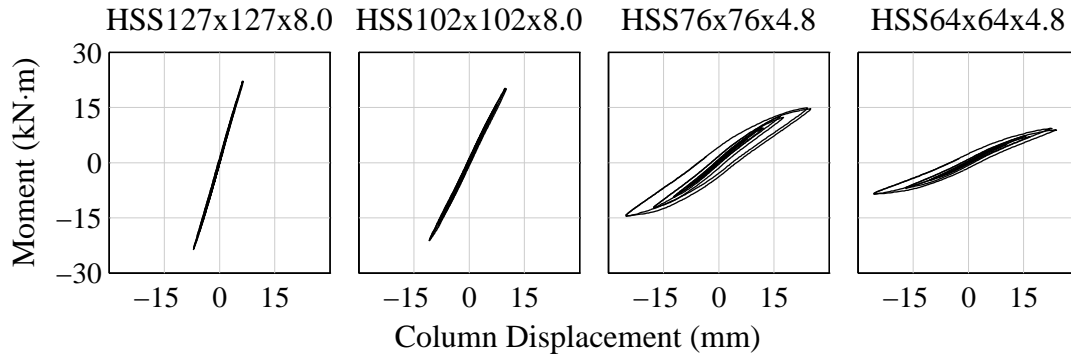


Figure 4.10: Moment-displacement hysteresses of each column

Yielding was observed in the HSS76x76x4.8 and HSS64x64x4.8 columns, while the HSS127x127x8.0 and HSS102x102x8.0 columns remained elastic. Figure 4.10 shows the moment-displacement hysteresses of each column specimen, where the moment is considered at the column end farthest from the bearing. The hysteresses indicate that only mild inelastic behaviour occurred in the columns that underwent yielding. The effect of the column yielding caused small permanent rotations at the column-bearing interface, leading to small bending moments at the bearing end at zero displacement. These effects can be observed in the bearing responses in Figures 4.7 and 4.8, which show wider hysteresses in the rotation and moment axes.

An interesting observation is the change in sign of the initial slope of the moment relationships between Figures 4.2, 4.5, and 4.6, and Figures 4.7 and 4.8. This effect can be understood by considering the moments that develop at the top of the bearing due to pure translation and pure rotation. For the case under positive translation with rotation fixed, a positive moment is required for equilibrium and the bearing is in double curvature (Figure 4.11 (a)). Conversely, under positive rotation with translation fixed, a negative moment is required for equilibrium and the bearing is in single curvature (Figure 4.11 (b)). For stiff subassemblies, rotations at the

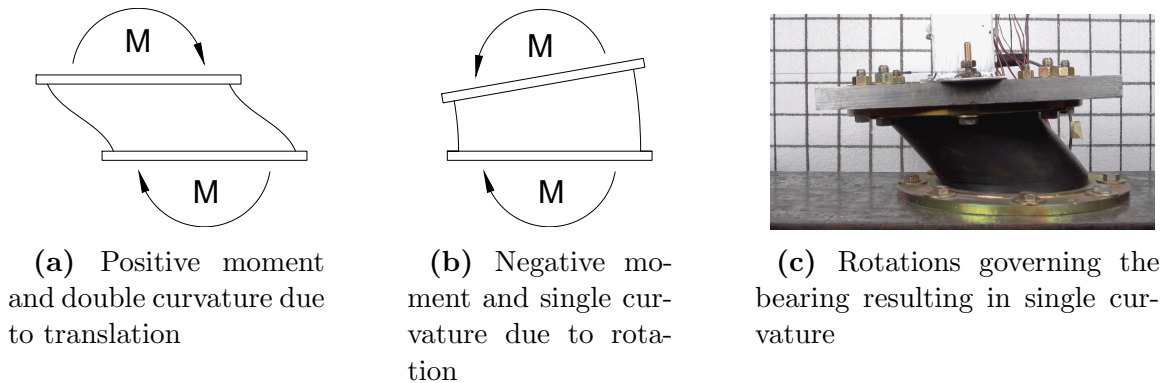


Figure 4.11: Moments and curvature cause by positive deformations

bearing end are small while translations are large, resulting in a positive moment. The bearing, being governed by the translation response, is then in double curvature with the inflection point of the subassembly located in the bearing. However, as the subassembly becomes flexible, rotations are larger while translations are smaller and the initial resulting moment is negative. This leads to the bearing being in single curvature, and the inflection point of the subassembly is located in the column.

This behaviour can be seen in the experimental bending moment diagrams in Figure 4.12, recorded at a displacement of 20 mm when the bearing was within the linear range. The stiffest subassembly resulted in a bending moment diagram similar

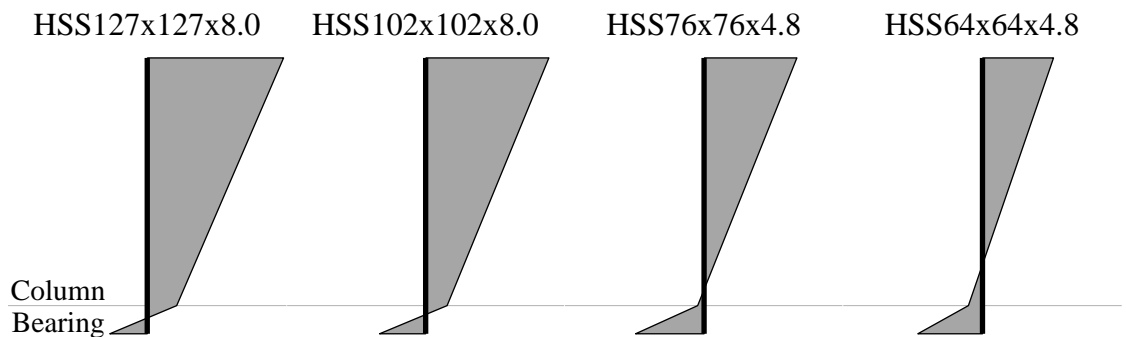


Figure 4.12: Bending moment diagrams at 20 mm displacement showing the progression of the inflection point with increasing column flexibility

to if the column were rigid, with the inflection point located near the middle of the bearing. As more flexible columns were installed in the subassembly, the inflection point under small displacements moved away from the midheight of the bearing and into the column. For the HSS76x76x4.8 subassembly, the inflection point was located near the column-bearing interface resulting in almost no moment at the bearing top, aligning with the results of the bearing moment shown in Figure 4.7 before nonlinear behaviour began. For moderately flexible columns, the moment at the column-bearing interface is small in comparison to the moment at the opposite end of the column, resulting in similar behaviour as a fixed-free column.

Assuming the moment-displacement relationship remains linear, as seen in Figure 4.2, the nonlinear behaviour of the bearing moment in Figures 4.6, 4.7, and 4.8 must then be attributed to a softening of the moment-rotation relationship. By fixing the degrees of freedom for rotation and translation at one end, the stiffness matrix of the bearing is of the form

$$\begin{bmatrix} V_2 \\ M_2 \end{bmatrix} = \begin{bmatrix} k_{33} & k_{34} \\ k_{43} & k_{44} \end{bmatrix} \begin{bmatrix} u_2 \\ \phi_2 \end{bmatrix} \quad (4.1)$$

The experimental results of the bearing without a column from Figure 4.2 can be used to obtain the k_{33} and k_{43} terms using the secant stiffness, as this test was conducted under pure translation with zero rotation of the endplates. The component of shear, V_θ , and moment, M_θ , due to rotation from testing of the subassemblies can then be isolated by

$$\begin{bmatrix} V_\theta \\ M_\theta \end{bmatrix} = \begin{bmatrix} V_2 - k_{33} \cdot u_2 \\ M_2 - k_{43} \cdot u_2 \end{bmatrix} = \begin{bmatrix} k_{34} \\ k_{44} \end{bmatrix} \begin{bmatrix} \phi_2 \end{bmatrix} \quad (4.2)$$

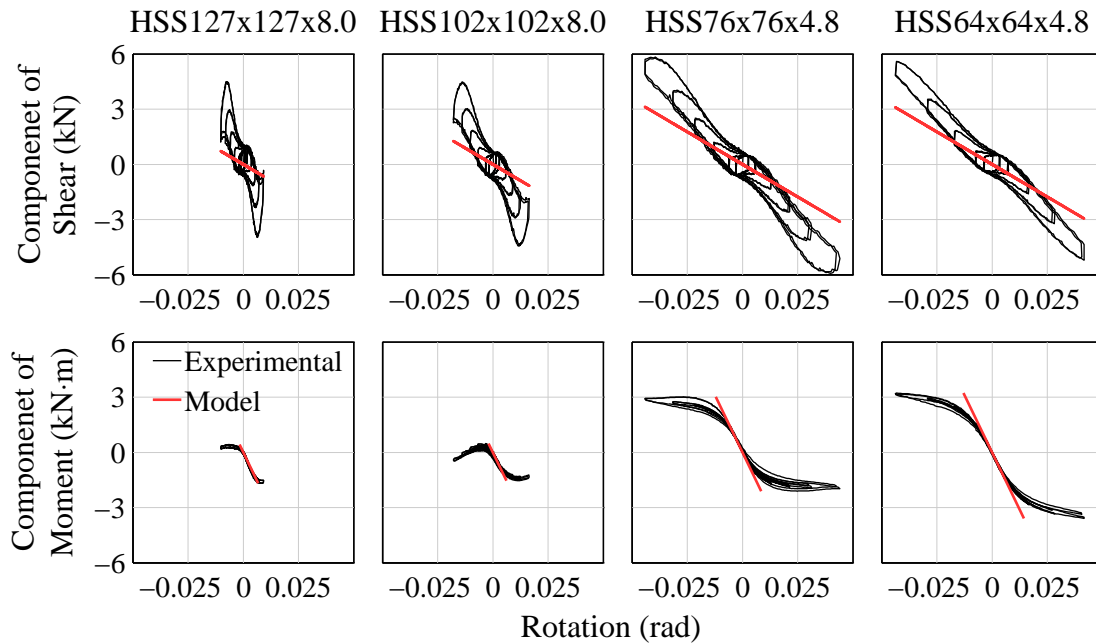


Figure 4.13: Components of the bearing shear and moment due to the bearing rotation only

where u_2 and ϕ_2 are the translations and rotations measured, and V_2 and M_2 are the shear and moment measured from the test under consideration. The results of this process are presented in Figure 4.13, comparing the components of shear and moment caused by rotation for each subassembly with the stiffness terms derived in the model. Both the shear-rotation and moment-rotation relationships are negative, which was indicated by the reduction of shear forces and bending moments when greater rotations were allowed at the column-bearing interface. Comparison with the derived stiffness terms shows good agreement with the initial moment-rotation stiffness, whereas the shear-rotation relationship is more accurate with more flexible columns. The changing stiffness of the experimental results for the shear-rotation relationship indicates a more complex relationship than solely a translational and rotational dependent term for determining the shear and moment. The experimental shear-rotation relationships are approximately linear; however, the moment-rotation

relationship shows repeatable elastic softening behaviour at rotations of 0.009 rad at the column-bearing interface. The analytical model is unable to account for this softening behaviour, limiting the range over which the model is reliable. The previous results of the bearing found the model to be accurate for the full range of shear strains when endplates remain parallel and up to $\pm 60\%$ shear strains when rotations exist. These findings are rooted in the amount of rotation experienced at the column-bearing interface as shown in this discussion and indicate the model is accurate when rotations are less than 0.009 rad at the column-bearing interface for the elastomeric bearing used in this study.

The high rotational stiffness of the columns compared to the bearing means that the rotation at the column-bearing interface is governed by the column size. By treating the column as a fixed-free structure, the relationship between the column displacements, Δ_c and the column-bearing interface rotations, θ can be found using Euler-Bernoulli beam theory as

$$\theta = \frac{3\Delta_c}{2L} \quad (4.3)$$

where L is the length of the column. Figure 4.14 shows that the relationship compares

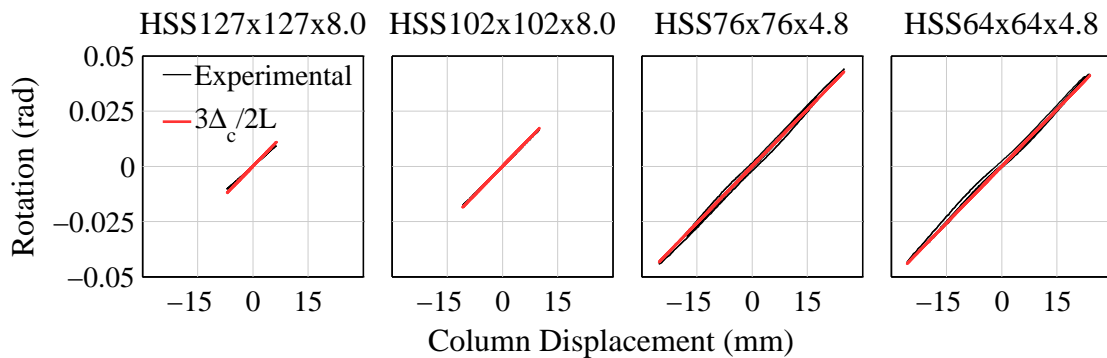


Figure 4.14: Column displacement and column-bearing interface rotation relationship

well to experimental results with the exception of the stiffest subassembly, where the relationship slightly over-estimated the rotations at the column-bearing interface. The discrepancy in the stiffest subassembly is due to shear deformations, not accounted for in Equation (4.3), which increase displacements without increasing rotations.

Figure 4.15 shows the effect of the stiffness ratio on the peak column displacement ratio and column base moment. The displacement ratio is a measure of the percentage of displacement demands the column experiences, and the base moment is considered at the column end farthest from the bearing where the largest bending moments occur. Since testing of the most flexible subassembly was stopped before the full displacement time history was conducted, the results shown are the peak values achieved at the ± 80 mm cycles for each test to make reasonable comparisons. To determine the column base moment when the stiffness ratio is zero, the forces obtained from the bearing-only test were used with equilibrium equations of a rigid column of equal length to the columns used in the experiment. The modelling closely follows the trends of the experimental results, but underestimates by a consistent amount. Experimental results show slightly higher displacements in the column than expected, which leads to the higher base moments. The larger experimental displacements are most likely

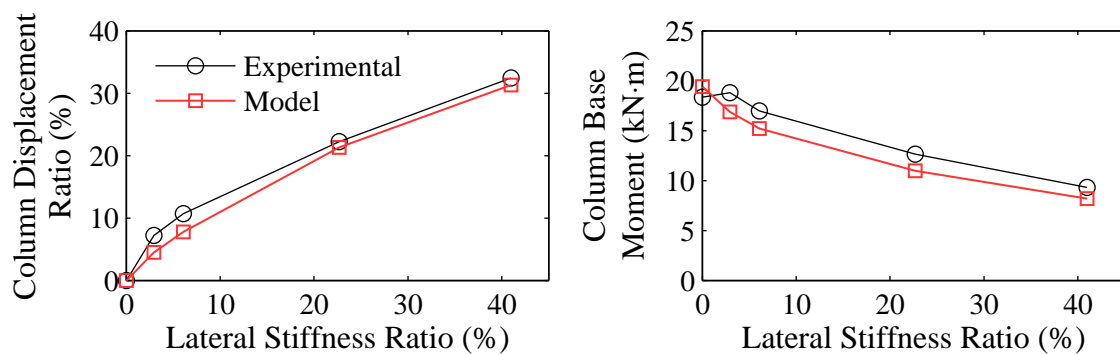


Figure 4.15: Effect of the stiffness ratio on the peak column displacement ratio and base moment

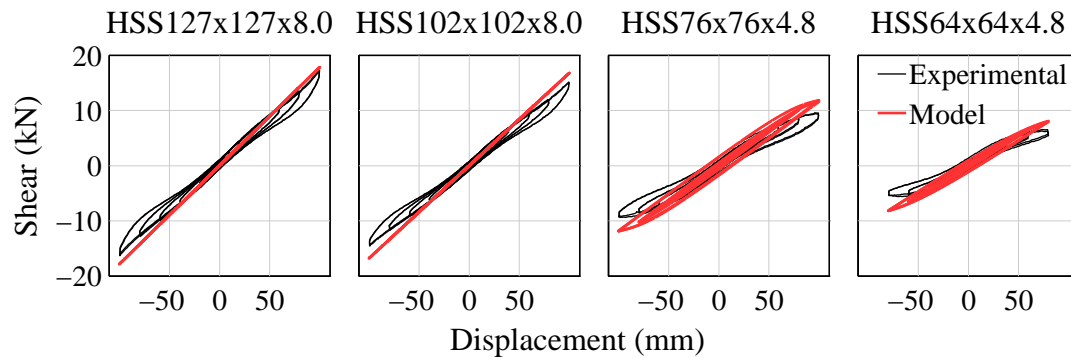


Figure 4.16: Global shear-displacement hysteresses of each subassembly

a result of softening in the moment-rotation relationship not characterized by the model. The softening causes the total moment at the bearing end to increase, leading to increased moments in the column and therefore larger displacements and base moments.

The global shear-displacement hysteresses for each subassembly tested are presented in Figure 4.16 to investigate the ability of the model to predict the lateral behaviour of the system despite not characterizing the softening of the bearing moment-rotation relationship. For the HSS127x127x8.0 subassembly, the model effectively predicted the lateral stiffness, but as the column became more flexible the model tended to overestimate the shear force at peak displacements as the nonlinear response of the bearing became more pronounced. Under small displacements, the lateral stiffness of the subassembly was effectively modelled as endplate rotations were still small and had not yet reached 0.009 rad when softening of the moment-rotation relationship began.

4.3 Post-Yield Response of a Column-Bearing Subassembly

To investigate the response of the bearing after the column has yielded, testing of the HSS76x76x4.8 subassembly was repeated. The second test followed the same displacement history prescribed in the first test, and the responses of the bearing are compared in Figure 4.17. A small shift is seen in the shear-rotation hysteresis indicating a permanent rotation at the column-bearing interface due to plastic deformations in the column. However, the permanent rotation was too small to have any significant influence on the lateral stiffness of the bearing or the moment at the column-bearing interface.

It should be noted that the HSS76x76x4.8 column only underwent small amounts of inelastic yielding, and that larger inelastic behaviour would likely influence the

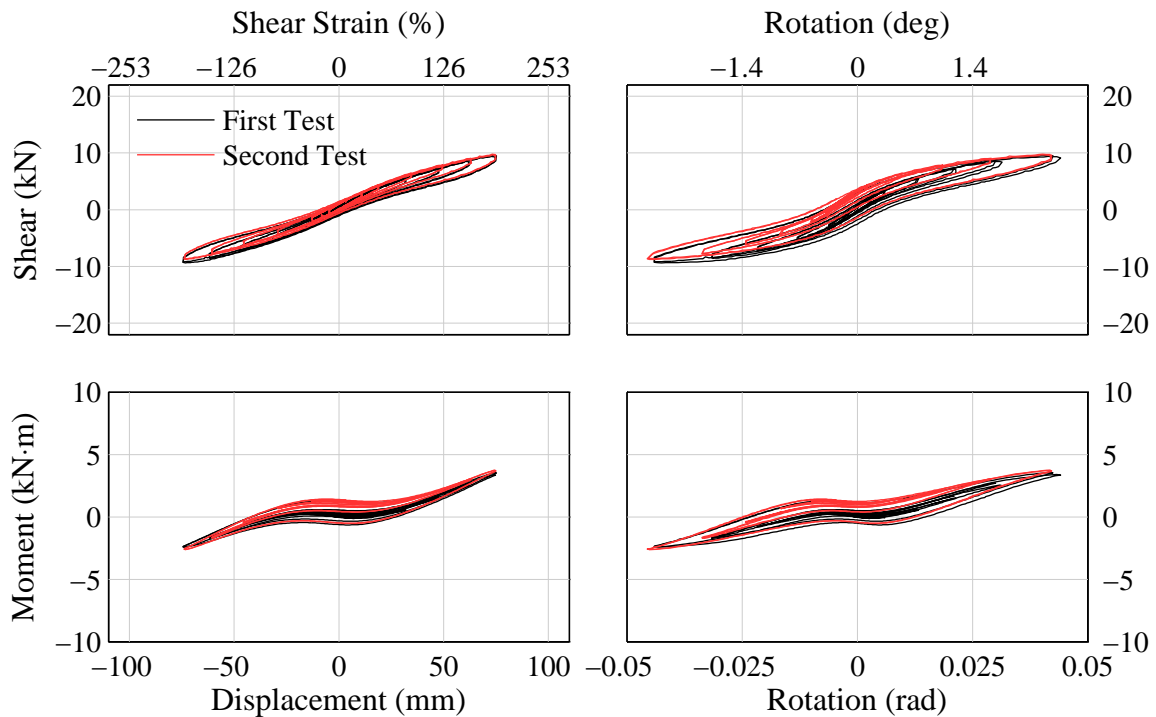


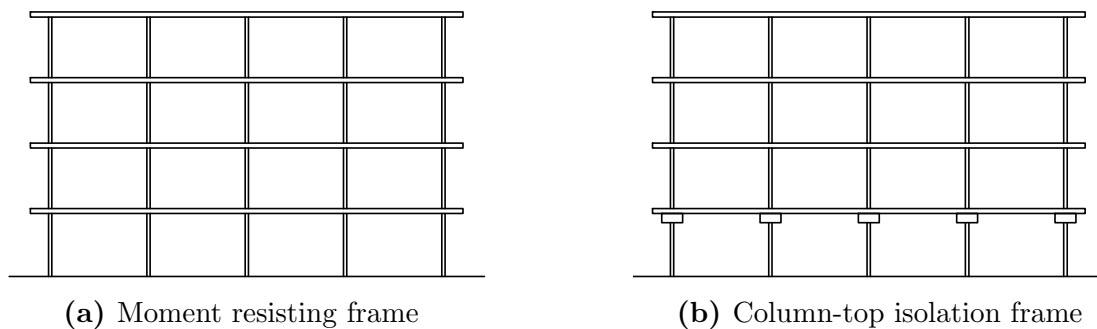
Figure 4.17: Post-yield response of the bearing in the HSS76x76x4.8 subassembly

response of the bearing. With larger plastic deformations, a larger shift in the rotation at the column-bearing interface would cause the lateral stiffness to increase or decrease depending on the direction of inelastic rotation. In addition, the shift in the rotation hysteresees would also cause a shift in the moment at the column-bearing interface. With large inelastic cycling of the column, strength degradation at the plastic hinge and overturning moments due to P- Δ effects would cause unstable performance of the supporting columns and must be avoided.

CHAPTER 5: PERFORMANCE AS A RETROFIT STRATEGY

5.1 Outline

In order to assess the viability of column-top isolation as a retrofit strategy, the performance of a typical office building designed to the 1965 National Building Code of Canada (NBCC) [15] was compared against the same building retrofit with column-top isolation. The building, theoretically positioned in Abbotsford, British Columbia, was designed as a steel moment resisting frame (MRF). For the retrofit, elastomeric isolators were designed to be placed at the tops of the first story columns with no additional retrofitting work to the frame members. Figure 5.1 presents the designed building for both the pre- and post-retrofit layouts. Suites of ground motions at hazard levels of 10% probability of exceedance in 50 years (design basis earthquake, DBE) and 2% probability of exceedance in 50 years (maximum considered earthquake, MCE) were selected and scaled to hazard levels prescribed in the 2010 NBCC [16]. Nonlinear time history analyses for the pre- and post-retrofit frame were conducted in OpenSees [25] using the bearing element derived in section 2.2.

**Figure 5.1:** Structural layouts of the original and retrofit frames

The following sections in this chapter will provide more details of the investigation by presenting the load provisions in the historical building code, detailing the building design and modelling, and comparing and discussing the results from the simulations on the effectiveness of column-top isolation for seismic retrofit.

5.2 Historical Structural Load Provisions

The 1965 National Building Code of Canada [15] was selected as the historical code used in this investigation due to the large amount of building stock from this era. For earthquake loading, the code prescribed a simple method of calculating the design base shear, V , as

$$V = K \cdot W \quad (5.1)$$

where K is termed as the minimum design load parameter and W is the seismic weight due to dead load plus any loads from storage, service equipment, and machinery. Determination of the minimum design load parameter consisted of several factors and is prescribed as

$$K = R \cdot C \cdot I \cdot F \cdot S \quad (5.2)$$

where R is the earthquake factor, C reflects the type of construction, I reflects the importance of the building, F reflects the foundation conditions, and S reflects the number of stories in the building.

The earthquake factor, R , attempted to capture the amount of hazard present at a given location and was determined from a seismic zoning map shown in Figure 5.2. The map was developed by Hodgson [28] using a qualitative assessment of the his-



Figure 5.2: Seismic zoning map in the 1965 National Building Code of Canada [15]

torical seismicity in Canada. He identified four zones based on the amount of seismic risk in each region. The earthquake factor was equal to the zone number that the building site was located in, with the exception of zone 3 along the west coast of British Columbia and the Ottawa-St. Lawrence valley region which was given an earthquake factor of 4.

The factor for the construction type, C , was used to capture the ductility available to particular structures. For steel or concrete moment resisting frames with rigid diaphragms and where the frame alone is able to carry 50% of the design shears, a value of 0.75 could be used. For any other types of construction used a value of 1.25 was assigned to the construction factor.

The importance factor, I , was used to increase the design values for structures which host large assemblies of people or with particular significance such as hospitals or power stations. For these structures, a value of 1.3 was to be used, while all other buildings could use an importance factor of 1.0.

The foundation factor, F , attempted to capture the amplification effects that can occur on soft soil sites. The factor was prescribed a value of 1.5 for building sites with highly compressible soil and 1.0 for all other soil conditions.

The story factor, S , was used to capture the effects that the structural period has by attributing this factor to the number of stories in the building. The factor was calculated as

$$S = \frac{0.25}{9 + N} \quad (5.3)$$

where N is the total number of stories in the building. The factor was not used to determine the building period, but rather to influence the design base shear by reducing the shear for taller buildings.

Once the design base shear was obtained, the code prescribed the shear to be distributed to each floor using

$$F_x = \frac{Vw_xh_x}{\sum w_xh_x} \quad (5.4)$$

where F_x is the lateral force at floor x , w_x is the seismic weight of floor x , and h_x is the height of floor x from the base.

Comparison of the historical seismic code to modern provisions and current understanding of site specific hazards shows the older provisions had an understanding of the key properties that influence hazard levels, albeit a rudimentary application based on broad factors. Further developments to the basis of the 1965 seismic provisions have led to the current requirements in the 2010 NBCC [16]. The most notable shift towards modern building codes is the use of site specific response spectra developed

through probabilistic seismic hazard analyses (PSHA) for a 2% probability of exceedance in 50 years. This change allowed better distinction of the hazards present between the broad seismic zones historically used, particularly with discerning the hazard differences between the west coast of British Columbia and the Ottawa-St. Lawrence valley region.

Wind loading in the 1965 code was prescribed using the climactic wind pressure, q_30 , available with the code for key cities. The pressure was increased along the height of the structure by multiplying the wind pressure by a factor dependent on the segment of the structural height under consideration. The various factors used to amplify the wind pressure are reproduced in Table 5.1.

Loading due to accumulation of snow followed a simple procedure based on modifying the ground snow load, a pressure available in the climactic data supplement for the code. The ground snow load was multiplied by a snow load coefficient, C_s , given as 0.8 for most applications. If the roof of the structure was exposed to direct winds and parapet walls or other building elements did not prevent snow from blowing off of the roof, the snow load coefficient could be reduced to 0.6.

Table 5.1: Wind amplification factor for height segments [15]

Height (ft)	Factor
0 - 40	1.0
40 - 60	1.1
60 - 90	1.2
90 - 130	1.3
130 - 190	1.4
190 - 270	1.5
270 - 420	1.6
420 - 740	1.8
740 - 1200	2.0

Load combinations in the code prescribed that all minimum design loads should be considered to act independently and simultaneously with the exception of wind and earthquake loading, which did not need to be considered to act simultaneously. No factors were used in load combinations, allowing 100% of all loads to act together.

5.3 Building Design and Modelling

A typical office building located in Abbotsford, British Columbia was selected for investigating the performance of a column-top isolation system as a retrofit strategy. The building, shown in Figure 5.1, was framed with steel members and used moment resisting frames as the lateral force resisting system. A footprint of four bays wide by eight bays long was used with 6 m spacing between columns in both directions, and four floors with 4 m heights were selected. Two moment resisting frames in both principal directions were assumed to be located on the perimeter of the building; however, for the purposes of this investigation only a single frame was considered for planar simulations. The selected four bay wide frame was designed according to loads prescribed in the 1965 NBCC [15].

A dead load of 3.6 kPa was assumed to act on the roof and 4.8 kPa on all other floors. Live loads for a roof were prescribed as 1 kPa and 2.4 kPa for all other floors used as office space. The ground snow load for a site in Abbotsford was prescribed as 2.4 kPa and a snow load coefficient of 0.8 was used leading to a snow load of 1.92 kPa. It was assumed that seismic loading governed the design of the moment resisting frame, so wind loading was neglected.

The site location of Abbotsford, British Columbia is specified to be in zone 3 on the seismic zoning map resulting in an earthquake factor of $R = 4$. The design of the

frame followed the provisions required to use a construction factor of $C = 0.75$. As a typical office building, the structure was given a normal importance resulting in $I = 1.0$. The site was assumed to have normal soil conditions, allowing a foundation factor of $F = 1.0$ to be used. Lastly, four stories were used in the equation prescribed to calculate a story factor of $S = 0.019$. These factors resulted in a minimum design load parameter of $K = 0.058$, meaning a base shear coefficient of 5.8%. Using the prescribed seismic weight, a base shear of 1196 kN was obtained. By comparison, the seismic load provisions in the 2010 NBCC [16] results in a base shear of 1520 kN, approximately 27% larger than the 1965 building code.

The base shear was distributed to each floor according to Equation (5.4), resulting in lateral forces of 199.4 kN, 199.4 kN, 132.9 kN, and 66.5 kN on the roof, 4th floor, 3rd floor, and 2nd floor, respectively, for a single moment resisting frame. The frame under consideration was analyzed using the portal method by assuming inflection points were located at the midspan of all beams and at the midheight of all columns. The frame was also modelled in SAP2000 structural analysis software to validate the design and load distribution. Load combinations of the dead, live, snow, and earthquake loads were used to determine peak demands in all members. The selected sections, summarized in Table 5.2, were designed based on design provisions in the

Table 5.2: Selected frame sections

Element	Section
Columns	W410x132
Gravity columns	W250x48
Second floor beams	W530x66
Third floor beams	W250x10
Fourth floor beams	W250x73
Roof beams	W310x33

CSA S16-14 steel code [29]. All members were assumed to have A36 grade steel with a yield strength of 250 MPa, based on the availability of steel products during the time period under consideration [30].

The historical code prescribed no limits to the lateral deflection, but specified that adequate stability must be provided. Modern interstory drift limits of 2.5% were used in place to provide stability of the structure; however, the design was governed by strength and so the drift limits were not required. The resulting fundamental period of the moment frame was 2.0 seconds, determined using the seismic weight defined by modern provisions which includes 25% of the snow load.

The structure was then retrofitted using a column-top isolation strategy by shortening the first story columns to accommodate elastomeric bearings without changing the floor heights. No other retrofitting work was prescribed for the frame, leaving all framing elements the same as the original moment resisting frame. The isolation system was designed using a conventional design process by assuming the endplates remain parallel, although it should be noted that the flexible end conditions will decrease the lateral stiffness of the bearings leading to a longer period than calculated. In addition, the buckling load of the bearings were determined assuming fixed-free conditions following the work by Imbimbo and Kelly [13] in order to provide a conservative estimate. Two different isolation bearings were designed for interior and perimeter columns to account for the different axial loads, but due to light loads on the bearings it was difficult to achieve a long isolation period. The bearings were assumed to have an incompressible rubber, and the relevant properties for the two designs are available in Table 5.3. Included in the table are the applied pressures on all the bearings along with the conservative buckling load. Maximum allowable

Table 5.3: Bearing design values. Note the applied pressure in parentheses is at the corner of the building.

Property	Perimeter	Internal
Radius (mm)	160	180
Rubber layer thickness (mm)	4.5	5.0
Total rubber thickness (mm)	112.5	125.0
Total height (mm)	202.5	215.0
Shape factor	17.8	18.0
Shear modulus (MPa)	0.4	0.4
Applied pressure (MPa)	4.13 (2.06)	6.53
Buckling pressure (MPa)	12.4	12.7

displacements were chosen as 300 mm to remain below 100% of the perimeter bearing diameter. The peak bearing displacements were expected to reach 221.8 mm based on the MCE level design spectrum. The resulting stiffness ratio for the perimeter column-bearing subassemblies was 4.8% and is comparable with the stiff subassemblies considered in the experimental program (see Table 3.2). With the bearings installed into the frame, the new fundamental period of the building was lengthened to 2.6 seconds.

Given the nonlinear behaviour of the bearing moment-rotation relationship discovered in section 4.2 which is not accounted for in the bearing model, results from this investigation should be interpreted with this in mind. However, considering the stiff columns used in this investigation, represented by the low stiffness ratio, numerical results of the column-bearing interaction are not expected to differ significantly from the real behaviour. It is expected that rotations of the bearing endplates will be small as a result of the stiff end conditions, resulting in a minor decrease in the lateral stiffness. It is also expected that the numerical results will slightly underestimate the displacements in the column and moments at the column base (see Figure 4.15).

Nonlinear time history analyses of the original MRF and retrofit frame were conducted using OpenSees [25]. All beams and columns were modelled with displacement based beam columns constructed with fiber sections representative of the wide flange elements selected for the design. The isolation bearings in the retrofit frame used the newly created element derived in section 2.2. The stress-strain behaviour of the steel was modelled with a Giuffr -Menegotto-Pinto hysteretic model using a yield strength of 250 MPa, a strain hardening ratio of 1%, and the shaping factors $R0 = 18$, $cR1 = 0.95$, and $cR2 = 0.4$. The shaping factors were selected to represent typical steel behaviour and were based on recommended values in the OpenSees command manual [25]. Lastly, a stiffness proportional damping ratio of 5% was assumed for the structure as well as the isolation system as elastomeric bearings tend to have low energy dissipation.

In order to capture the proper distribution of mass and stiffness within the retrofit building due to the weaker internal gravity frames, the entire retrofit building was modelled. This included two original moment resisting frames at each end of the building with seven gravity frames in between, all connected by rigid diaphragms at each floor. The original lateral force resisting frames in the other principal direction of the building were ignored, and so all gravity frames were modelled only with the gravity columns outlined in Table 5.2. For the purposes of this study, only the behaviour of the perimeter frame (originally the moment resisting frame) is considered to compare the original and retrofit structures.

5.4 Ground Motion Selection and Scaling

Ground motions for use in the nonlinear time history analyses were selected and scaled based on current understanding of the seismic hazards present in Abbotsford.

Deaggregation maps for both the DBE and MCE hazard levels were used to determine the expected magnitudes and distances from seismic events present at a site in Abbotsford. Both hazard level maps indicated a mean magnitude of 6.5 to 8.0 at a distance of less than 100 km for the majority of the hazards in the 0.5 to 3 second period range. Suites of ground motions with these criteria were obtained for the DBE and MCE levels using the PEER ground motion database [31] and are listed in Table 5.4 with the scaling factors used.

Scaling of the ground motions followed the provisions outlined by the American Society of Civil Engineers (ASCE) 7-05 [32] to match the design spectrum for Abbotsford, prescribed in the 2010 NBCC [16]. The ASCE guidelines specify ground motions should be scaled on the period range of 0.2 to 1.5 times the fundamental period for typical nonlinear response history analyses and 0.5 to 1.25 times the fundamental period for isolated buildings. In order to meet the requirements to allow the same ground motions to be used on both frames, a scaling range of 0.2 times the period of the moment resisting frame to 1.25 times the period of the isolated frame was used, resulting in a range of 0.4 to 3.25 seconds. Scaling was conducted so that the average

Table 5.4: Selected ground motions for nonlinear time history analyses

Earthquake	Year	Station	Magnitude	Scale Factor
DBE				
Imperial Valley	1979	Cerro Prieto	6.5	1.513
San Fernando	1971	Palmdale Fire Station	6.6	1.457
Kern County	1952	Santa Barbara Courthouse	7.4	1.438
Landers	1992	Barstow	7.3	1.565
MCE				
Loma Prieta	1989	Palo Alto-SLAC Lab	6.9	1.477
Landers	1992	Joshua Tree	7.3	1.429
Corinth	1981	Corinth	6.6	1.684
Cape Mendocino	1992	Petrolia	7.0	1.056

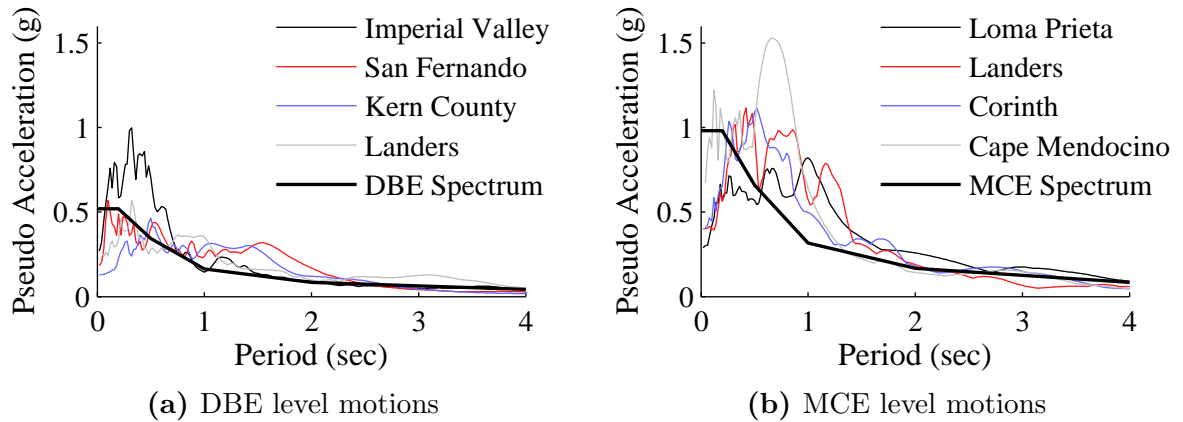


Figure 5.3: 5% Damped response spectra of selected ground motions

response spectrum of the four DBE ground motions was not less than the DBE design spectrum at any point in the scaling range, and a similar process was done for the MCE ground motions. The response spectra of the scaled ground motions selected for this investigation can be viewed in Figure 5.3 with comparisons of the design spectra for each hazard level considered.

5.5 Numerical Results

The global behaviour of both the pre-retrofit MRF and the retrofit frame was investigated to assess the performance of a column-top isolation system as a retrofit strategy. The peak interstory drifts and floor accelerations under the DBE and MCE ground motions are presented in Figures 5.4 and 5.5, respectively. It is important to note that the interstory drifts of the first floor in the retrofit frame are considered as the drift experienced by the supporting column underneath the bearing, rather than the drift between the first and second floors. In this way, the drifts are representative of the demands on the columns and are not increased by the large displacements expected in the isolation layer. Peak interstory drifts in the original MRF under the MCE motions exceeded those expected during the design process as a result of the

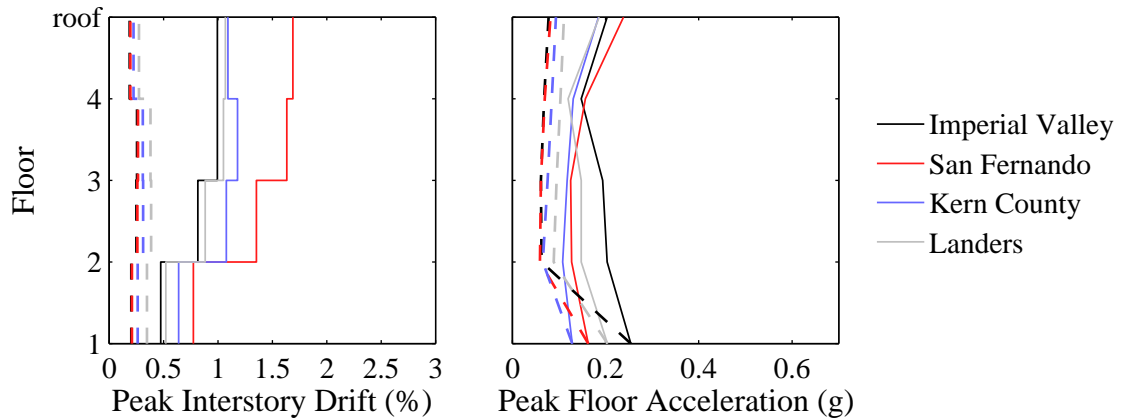


Figure 5.4: Peak interstory drifts and floor accelerations during the DBE motions. Solid lines represent the original MRF and dashed lines represent the retrofit frame.

low estimate of the base shear determined from the historical code provisions. Peak floor accelerations in the original MRF during the MCE level motions showed low peak accelerations on the fourth floor with higher accelerations on all other floors, indicating the presence of higher mode effects. Comparison to the retrofit frame shows the higher mode effects were significantly reduced once the isolation layer was installed.

As a result of the long period of the original MRF, peak floor accelerations during

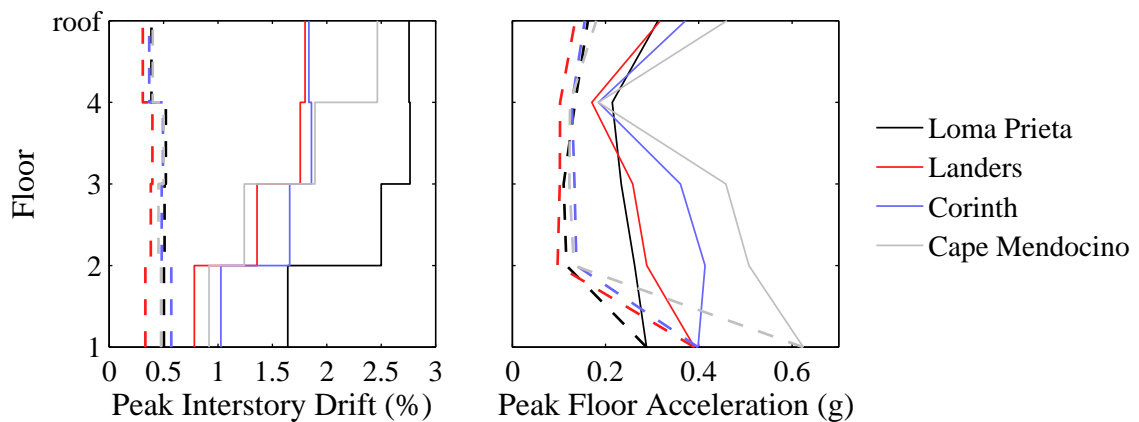


Figure 5.5: Peak interstory drifts and floor accelerations during the MCE motions. Solid lines represent the original MRF and dashed lines represent the retrofit frame.

the DBE motions were relatively low. However, the retrofit strategy was still able to provide effective reductions for both peak interstory drifts and floor accelerations. Peak interstory drifts in the retrofitted frame were reduced by approximately 70% on average under both DBE and MCE motions when compared with the original retrofit frame. The retrofit also achieved average reductions in the peak floor accelerations above the first floor by 48% under the DBE motions and 55% under the MCE motions.

Yielding of the original MRF was observed in all ground motions except for the DBE level Imperial Valley and Landers motions. In contrast, the retrofit frame experienced no yielding for any of the ground motions (DBE or MCE) used in this investigation. Comparisons of the pre- and post-retrofit moment-rotation hysteresses for beams on each floor of the frame are presented in Figure 5.6 for the MCE level Loma Prieta motion. The hysteresses show that yielding in the MRF occurred throughout the frame while the retrofit frame only showed minor elastic demands on the beams.

Of particular concern for a column-top isolation system are the demands on the supporting column, which should avoid yielding to prevent the formation of plastic hinges and in turn a soft story collapse mechanism. The peak bending moments

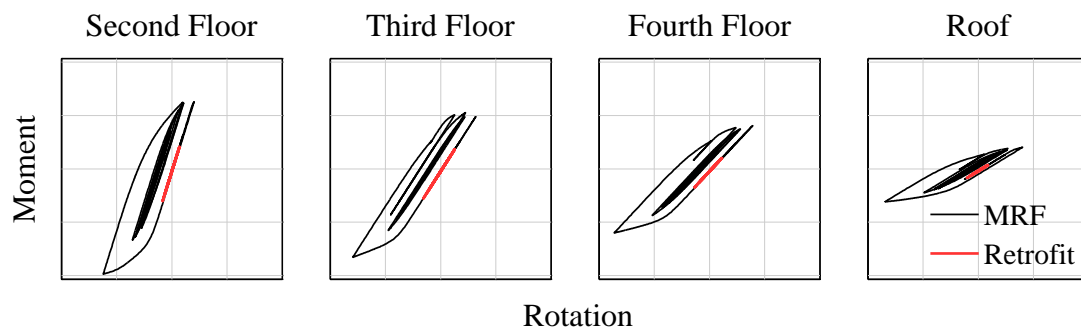


Figure 5.6: Comparison of the pre- and post-retrofit moment-rotation hysteresses for beams on each floor during the MCE Loma Prieta motion

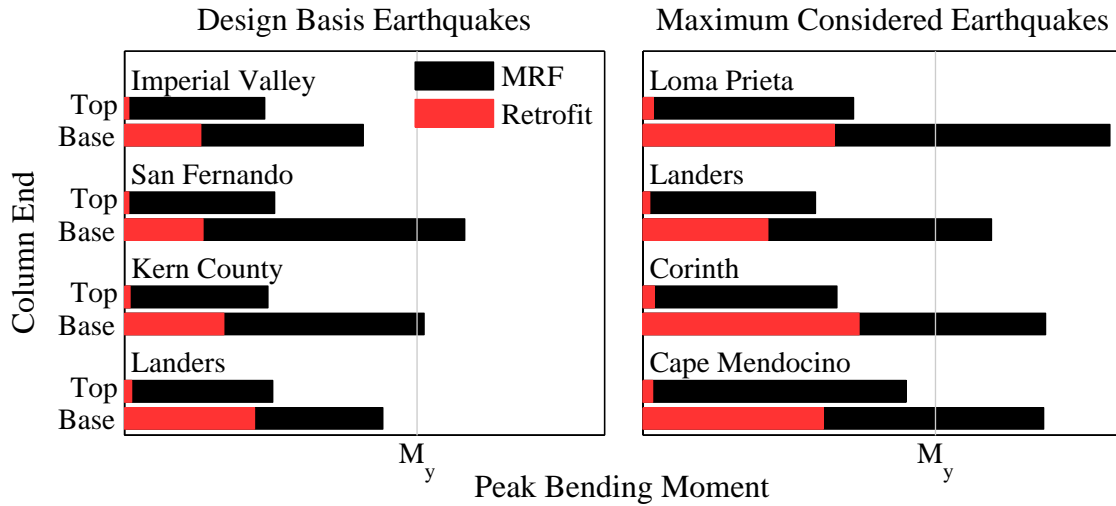


Figure 5.7: Comparison of the peak moments in the first story columns

that occurred at the top and base of the first story columns for all ground motions are presented in Figure 5.7, with comparisons between the original MFR and retrofit frames. The yield moment, M_y , of the columns is also included in the figure for reference. Peak bending moments in the retrofit frame were largest at the base of the column; however, these moments remained in the elastic range. Peak moments at the base of the column were reduced on average by 64% under the DBE motions and 55% under the MCE motions. Of note is the significant reduction in peak moment at the top of the column once the isolation system was installed due to the relatively small bending moment transmitted through the elastomeric bearings. Peak moments at the tops of the first story columns achieved a mean reduction of 95% under both DBE and MCE motions with the retrofit strategy.

The large reduction in bending moments at the tops of the first story columns in comparison to the reduction at the base indicates a redistribution of forces within the structure once the isolation system is installed. To investigate this, the peak elastic bending moment diagram for the entire structure is examined in Figure 5.8 for the

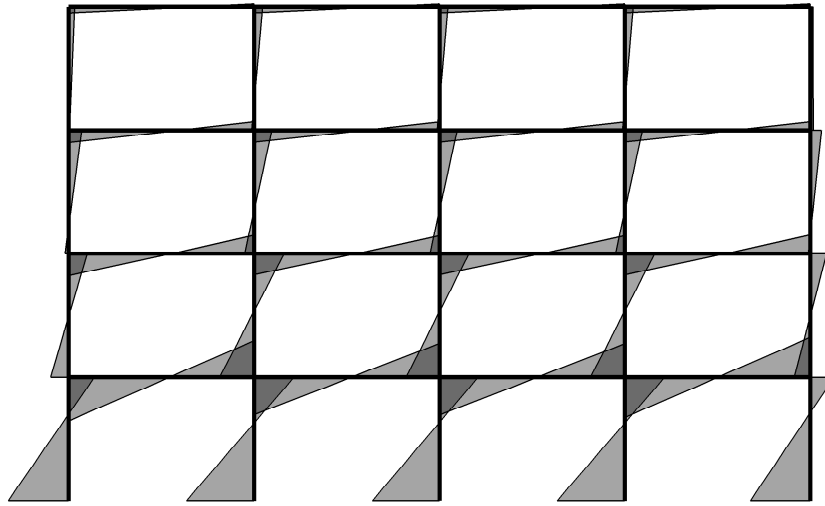


Figure 5.8: Peak elastic bending moment diagram in the original MRF during the DBE level Imperial Valley motion

pre-retrofit MRF during the DBE level Imperial Valley motion. The diagram shows a typical distribution of bending moments throughout the structure for a moment resisting frame, with the largest bending moments occurring at the base of the inner first story columns and second floor beams. The first story columns on the outside of the frame had slightly lower base moments than the inner columns as a result of lower shears in the outer columns.

In comparison to the MRF bending moment diagram, Figure 5.9 shows the peak bending moment diagram for the retrofit frame during the DBE level Imperial Valley motion on the same scale used in Figure 5.8. The most noticeable difference in the retrofit frame is the reduction of bending moments in the frame as a result of a longer fundamental period and a concentration of displacements to the isolation layer. In addition to this, the shears in the superstructure evenly distributed through the isolation layer resulting in nearly equal demands on all first story columns. P- Δ moments on the columns caused small variations in the moment between the inner and

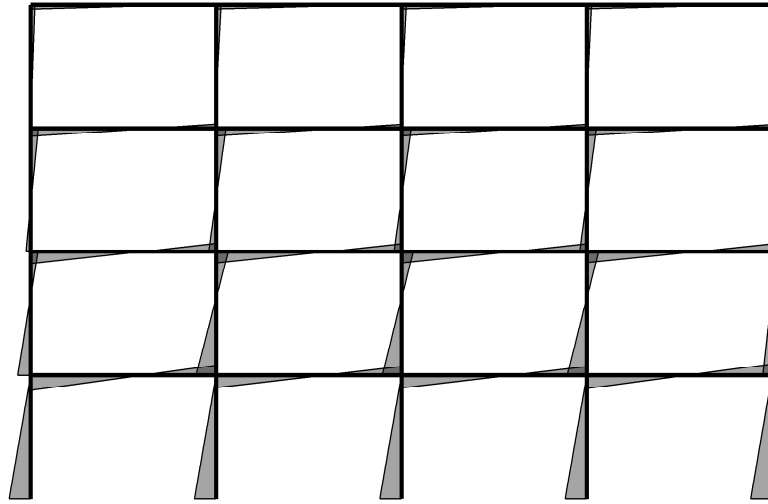


Figure 5.9: Peak elastic bending moment diagram in the retrofit during the DBE level Imperial Valley motion

outer columns of the frame because of differing axial loads; however, these moments were negligible in comparison to the moments caused by the shears at the tops of the columns.

The bending moment diagram for the retrofit frame also highlights that the first story columns have similar bending moments to cantilever structures. In this sense, supporting columns act as fixed-free structures, reducing the lateral stiffness and buckling load from the previous MRF configuration. For the frame investigated in this study, all first story columns in the MRF were chosen to use the same section and were originally designed for the large axial forces transmitted into the outer columns from the shear forces in the second floor beams. Once the isolation system was installed, columns in the retrofit frame experienced significantly lower axial demands due to smaller shears in the second floor beams. As a result, the decrease in the buckling load capacity of the columns was counteracted with a decrease in axial loads; thus, buckling of the first story columns was not an issue.

Deformations of the isolation bearings were recorded to study the rotations at both the top and bottom endplates along with the lateral displacements for each motion. Rotations of the top plates were expected to be smaller than the bottom plate rotations due to differences in the end conditions above and below the bearings. Above the isolation layer, bearing top plates connected to beams and columns within the superstructure, providing stiffer connections than the bearing bottom plates which connected to only a single column in the substructure. This can be observed in Figure 5.10, presenting the time history of the deformations in a bearing on the corner of the building for the MCE level Loma Prieta motion. By comparison, Figure 5.11 shows the response of a bearing in the center of the frame under consideration during the same motion. The center bearing experienced even lower rotations of the top plate than the corner bearing due to an additional beam connecting above the center bearing providing a stiffer end condition. Peak bottom plate rotations and lateral displacements were the same for both bearings, further confirming that supporting columns experienced similar demands regardless of the location in the frame. Typ-

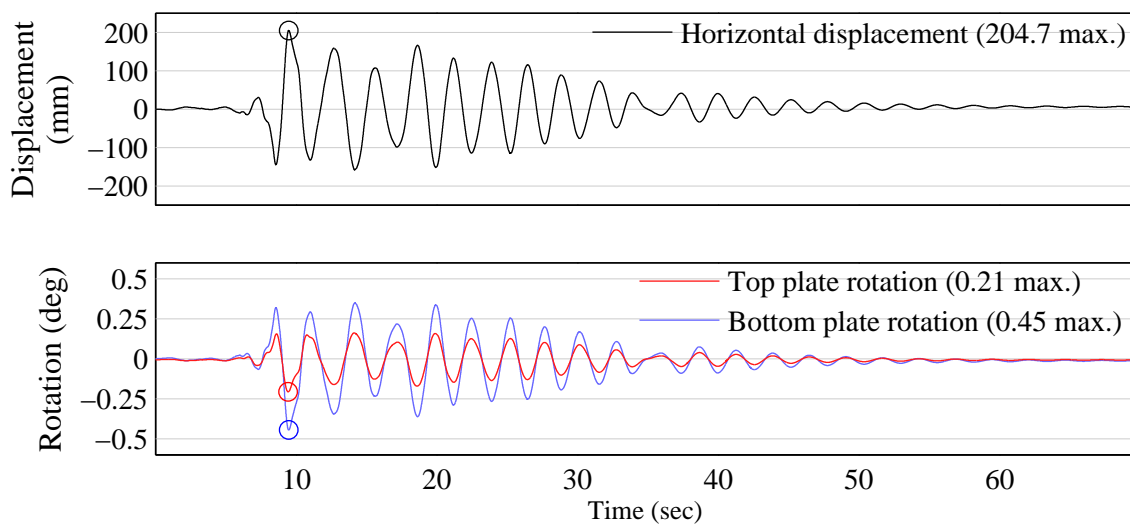


Figure 5.10: Response time history of a corner bearing during the MCE level Loma Prieta motion

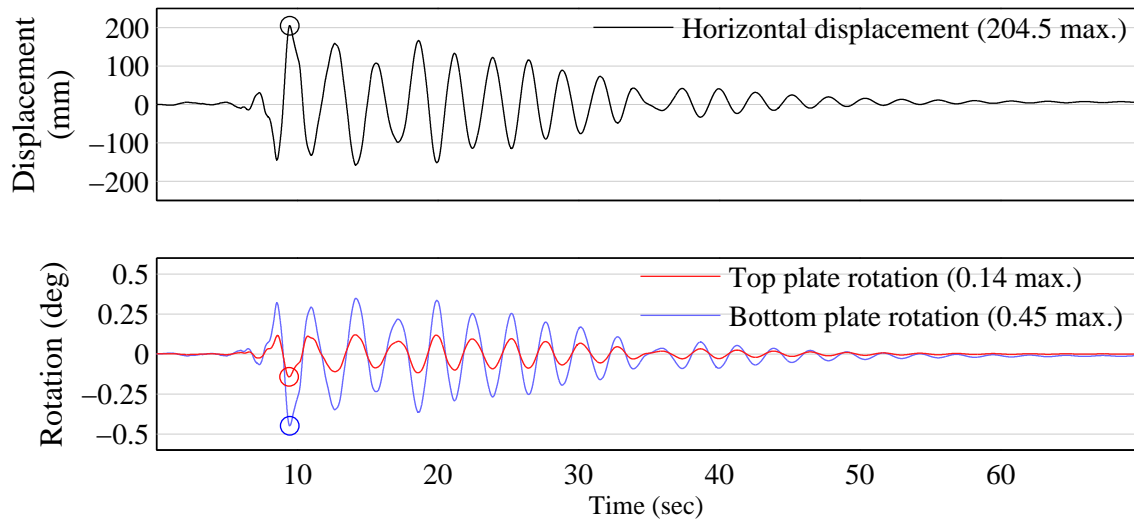


Figure 5.11: Response time history of a center bearing during the MCE level Loma Prieta motion

ically it would be expected that the differences in top plate rotations would affect the lateral stiffness of the bearings and therefore the lateral displacement; however, rotations of these endplates were small resulting in negligible influence on the lateral behaviour. Rotations of the bottom plates, although larger than the top plate rotations, were relatively small as well, indicating that the supporting columns were able to provide stiff boundary conditions for the bearings even without substructure upgrades during the retrofit.

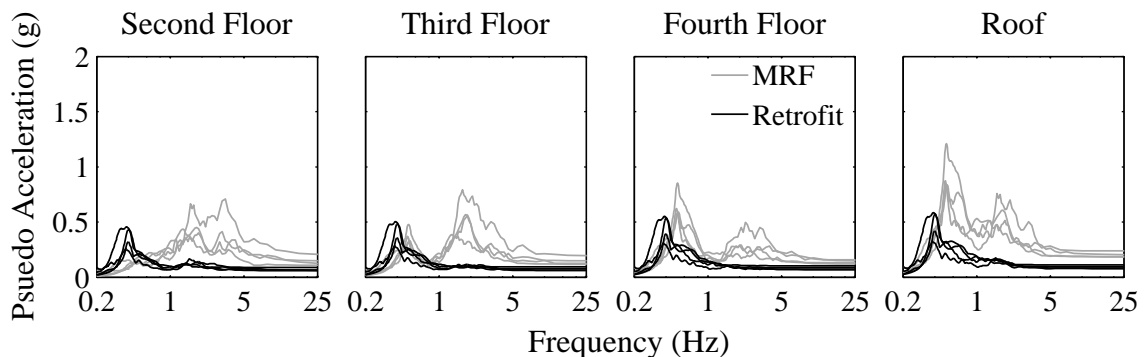
Peak rotations of the top and bottom endplates and peak lateral displacements for all of the MCE level motions are provided in Table 5.5. Peak lateral displacements of the bearings remained under the maximum allowable displacement of 300 mm, and most motions remained under the expected MCE displacement of 221.8 mm with the exception of the Corinth motion, which resulted in a peak displacement of 231.8 mm. The higher lateral displacement than expected is attributed to the long period content of the Corinth motion around the fundamental period of 2.6 seconds, as observed in

Table 5.5: Peak bearing responses during the MCE level motions

Earthquake	Disp. (mm)	Top Rot. (deg)	Bottom Rot. (deg)
Loma Prieta	204.7	0.207	0.451
Landers	133.7	0.157	0.295
Corinth	231.8	0.198	0.510
Cape Mendocino	193.3	0.186	0.425

the response spectrum in Figure 5.3 (b).

Within the superstructure, floor specific response spectra were computed assuming 5% damping to compare the effects of the retrofit strategy on building equipment and contents. The floor spectra for the DBE level motions, shown in Figure 5.12, show the retrofit frame had a smaller range of frequencies where the majority of the excitation was concentrated when compared with the original MRF. In addition, the frequency range for the retrofit frame is at a lower frequency than the original MRF and is outside of the typical resonant range of 2-5 Hz for equipment and contents. The magnitude of the maximum spectral acceleration on all floors was relatively unchanged except for the roof which saw significant decreases. Figure 5.13 presents the floor spectra during the MCE level motions and shows a similar reduction in bandwidth and shift to the low frequency region. A second peak around 1.5 Hz begins

**Figure 5.12:** 5% Damped floor response spectra for the DBE level motions

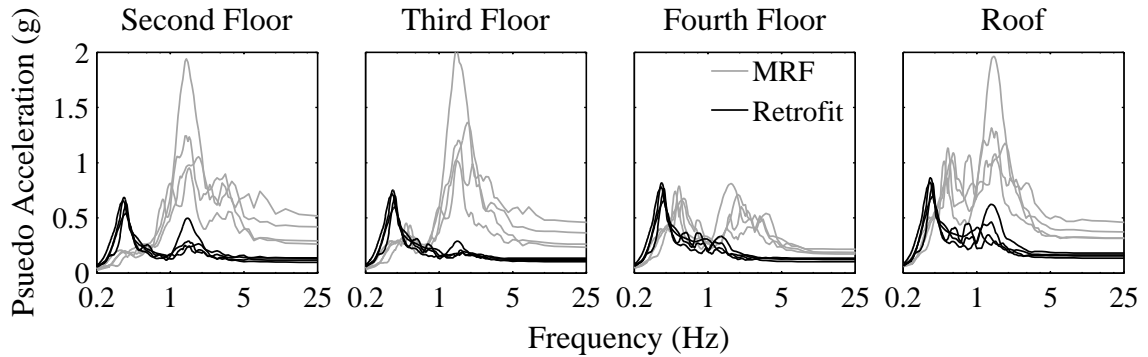


Figure 5.13: 5% Damped floor response spectra for the MCE level motions

to form across all floors in the retrofit frame, attributed to the second mode of the retrofit frame which had a period of 0.65 seconds. Maximum spectral accelerations were significantly reduced in the second, third and roof levels, while the fourth floor had negligible differences due to the relatively low accelerations in the original MRF because of the higher mode effects discussed previously. Overall, the retrofit strategy showed to significantly decrease the demands on non-structural equipment and building contents through the combined effects of a narrowing and lower frequency range in comparison to the original MRF.

CHAPTER 6: CONCLUSIONS AND RECOMMENDATIONS

6.1 Conclusions

While seismic isolation has been shown to significantly improve the seismic performance of new and existing buildings by effectively reducing both interstory drifts and floor accelerations, applications tend to be limited to buildings with historical or functional significance because of large costs associated with traditional isolation. These costs are further exacerbated in retrofit applications, which often require significant foundation work to accommodate the isolation bearings. By placing the bearings on the tops of columns, project costs can be reduced by eliminating design elements which contribute significant expenses. However, supporting columns beneath the isolation layer may not provide rigid boundary conditions to the bearings, resulting in endplates not remaining parallel. Previous theoretical studies have shown that endplate rotations can affect the lateral stiffness and stability of elastomeric bearings, but have focused on constant rotations or fixed-free conditions. In addition, the previous studies assumed that bearings are made of incompressible rubber, limiting applications to rubbers with high bulk modulus to shear modulus ratios.

To investigate the effects of endplate rotation on the response of elastomeric bearings when subjected to varying endplate flexibilities, a model was developed based on Haringx's theory and includes the effects of compressible rubbers. The model described an elastomeric bearing with a simple stiffness matrix consisting of translational and rotational degrees of freedom at both endplates. To validate the model, an experi-

mental program was conducted on column-bearing subassemblies under quasi-static cyclic testing. Four steel columns with varying section sizes were tested in the subassemblies to examine a range of flexibility and strength limits. Numerical simulations of the experimental setup were performed using the bearing model, and results were compared with experimental findings. The following conclusions are drawn from the experimental program:

- Flexible boundary conditions can significantly reduce the lateral stiffness of elastomeric bearings due to the presence of endplate rotations. As endplate rotations increased, nonlinear elastic softening was observed in the moment-rotation relationship leading to larger endplate rotations and further decreases in the lateral stiffness than expected. The bearing model accurately predicted the bearing responses when endplate rotations were small; however, as the model does not characterize the nonlinear behaviour in the moment-rotation relationship, numerical results diverged from experimental results at larger endplate rotations.
- The bending moment diagrams from the experimental data show that the columns tend to have small moments at the column-bearing interface due to a low ability of the bearing to transmit moment. Shear forces transmitted through the bearing tended to govern the bending moments in the column, resulting in the columns behaving similarly to fixed-free structures.
- For a rigid column, the inflection point of the subassembly should theoretically be located at the midheight of the bearing, while an infinitely flexible column should have the inflection point at the midheight of the column. The transition of the inflection point was observed experimentally in the linear range

of the bearing, with the stiffest column providing near rigid conditions. As the column became more flexible, the inflection point began to move away from the bearing midheight. For the most flexible column, the inflection point moved beyond the column-bearing interface and into the column, resulting in the bearing undergoing single curvature.

- The column stiffness governs the rotation at the column-bearing interface, and a simple relationship between the column displacement and the bearing-column interface rotation can be found by approximating the column as a fixed-free structure using Euler-Bernoulli beam theory.

To investigate the performance of a column-top isolation system as a retrofit strategy, nonlinear time history analyses were conducted to compare the pre- and post-retrofit performance of a moment resisting frame located in Abbotsford, British Columbia. The original frame was designed according to load provisions in the 1965 National Building Code of Canada to represent a typical office building constructed in that era and was retrofitted with elastomeric bearings on the tops of the first floor column with no additional retrofitting work to the frame. Both frames were simulated under suites of ground motions at the DBE and MCE hazard levels based on seismic hazards prescribed in the 2010 National Building Code of Canada. Results of the two frames were compared to determine the following conclusions:

- The installation of a column-top isolation system provided large reductions to the peak interstory drifts and floor accelerations observed in the original MRF. Peak interstory drifts were reduced by 70% for both DBE and MCE level motions, and peak floor accelerations were reduced by 48% for the DBE and 55% for the MCE level motions. Yielding was shown to occur throughout

the MRF leading to peak interstory drifts as high as 2.8%, while only minor elastic demands occurred in the retrofit frame reaching a maximum drift of 0.6%.

- Due to the limited ability of the bearings to transmit moment from the superstructure into the substructure, supporting columns acted as fixed-free structures. Although the buckling load of the columns is reduced in this configuration, there were lower axial forces in the retrofit design due to reduced overturning moments from smaller accelerations.
- Peak endplate rotations varied depending on the location in the frame; however, rotations were small due to relatively stiff supporting columns in the original MRF.
- The floor response spectra for the retrofit building had peaks within a lower frequency range, closer to the isolation layer frequency, than for the original MRF. The retrofit moved the frequency range of the floor accelerations away from the dominant frequencies of most building equipment and contents. As a result, the performance of building content and equipment would likely be improved using the retrofit strategy.

6.2 Recommendations for Future Work

Through the course of this work on flexible end conditions for elastomeric bearings and the behaviour of column-top isolation systems, several areas have been identified that require further investigation to continue this body of research. The following recommendations are provided for areas of future work:

- Experimental results of the elastomeric bearing while endplates rotate showed that the moment response was nonlinear. The moment-rotation hystereses indicated elastic softening occurred in this relationship; however, this relationship was extracted assuming the moment-displacement relationship remained unchanged when rotations were present. An experimental investigation testing an elastomeric bearing under pure rotation would be beneficial to affirm this behaviour. In addition, modification of the bearing model to account for the nonlinear response would allow better prediction of elastomeric bearings subjected to flexible end conditions.
- As the response of elastomeric bearings can be sensitive to strain-rate, dynamic testing of column-bearing subassemblies may provide insight into the performance of these systems in more realistic scenarios.
- A comprehensive cost analysis of the implementation of a column-top isolation system for both new construction and retrofit projects would aid in expressing the benefits of using this type of isolation system. Some information about the cost benefits was obtained through communications with practitioners; however, more research is required to quantify the monetary benefits.

REFERENCES

- [1] S. Taghavi and E. Miranda, “Response assessment of nonstructural building elements,” Tech. Rep. PEER-2003/05, Pacific Earthquake Engineering Research Center, 2003.
- [2] V. A. Matsagar and R. S. Jangid, “Base isolation for seismic retrofitting of structures,” *Practice Periodical on Structural Design and Construction*, vol. 13, no. 4, pp. 175–185, 2008.
- [3] FEMA, *FEMA-273: Guidelines for the Seismic Rehabilitation of Buildings*. Federal Emergency Management Agency, 1997.
- [4] J. M. Kelly, *Earthquake Resistant Design with Rubber*. London: Springer-Verlag, 1993.
- [5] M. Nakai, “Preservation and restoration of tokyo station marunouchi building,” *Japan Railway & Transport Review*, no. 61, p. 10, 2013.
- [6] T. C. Becker and S. A. Mahin, “Effect of support rotation on triple friction pendulum bearing behavior,” *Earthquake Engineering and Structural Dynamics*, vol. 42, no. 12, pp. 1731–1748, 2013.
- [7] G. Mosqueda, A. S. Whittaker, G. L. Fenves, and S. A. Mahin, “Experimental and analytical studies of the friction pendulum system for the seismic protection of simple bridges,” Tech. Rep. EERC 2004-01, Earthquake Engineering Research Center, 2004.
- [8] A. Karbakhsh Ravari, I. B. Othman, Z. B. Ibrahim, and K. Ab-Malek, “P- Δ and end rotation effects on the influence of mechanical properties of elastomeric isolation bearings,” *Journal of Structural Engineering*, vol. 138, no. 6, pp. 669–675, 2012.

-
- [9] S. Rastgoo Moghadam and D. Konstantinidis, “Effect of rotation on the horizontal behaviour of rubber isolators,” in *11th Canadian Conference on Earthquake Engineering*, pp. 1–10, 2015.
- [10] K. Tamura, Y. Nakamura, and T. Saito, “A new base-isolated long-span structure overhanging urban infrastructure,” in *Council on Tall Buildings and Urban Habitat: Seoul Conference*, (Seoul, Korea), pp. 1–17, 2004.
- [11] D. Pettinga and S. Oliver, “Aspects of design for the base isolated christchurch justice and emergency services precinct,” in *10th Pacific Conference on Earthquake Engineering*, (Sydney, Australia), pp. 1–8, 2015.
- [12] N. M. Post, “Seismic engineer develops ‘showcase’ for isolators,” *Engineering News-Record*, August 2015.
- [13] M. Imbimbo and J. M. Kelly, “Stability aspects of elastomeric isolators,” *Earthquake Spectra*, vol. 13, no. 3, pp. 431–449, 1997.
- [14] C. Chang, “Modeling of laminated rubber bearings using an analytical stiffness matrix,” *International Journal of Solids and Structures*, vol. 39, no. 24, pp. 6055–6078, 2002.
- [15] NRCC, *National Building Code of Canada*. National Research Council Canada, Ottawa, 1965.
- [16] NRCC, *National Building Code of Canada*. National Research Council Canada, Ottawa, 2010.
- [17] J. A. Haringx, “On highly compressible helical springs and rubber rods, and their application for vibration-free mountings, III,” Tech. Rep. 4, Philips Research Reports, 1949.
- [18] A. N. Gent and E. A. Meinecke, “Compression, bending, and shear of bonded rubber blocks,” *Polymer Engineering and Science*, vol. 10, no. 1, pp. 48–53, 1970.
- [19] C. J. Derham and A. G. Thomas, “The design of seismic isolation bearings,” in

Control of Seismic Response of Piping Systems and Other Structures by Base Isolation, pp. 21–32, Berkeley: University of California, 1981.

- [20] J. F. Stanton, G. Scroggins, A. W. Taylor, and C. W. Roeder, “Stability of laminated elastomeric bearings,” *Journal of Engineering Mechanics*, vol. 116, no. 6, pp. 1351–1371, 1990.
- [21] C. G. Koh and J. M. Kelly, “Effects of axial load on elastomeric isolation bearings,” Tech. Rep. UCB/EERC-86/12, Earthquake Engineering Research Center, Berkeley, 1987.
- [22] H. C. Tsai and S. J. Hsueh, “Mechanical properties of isolation bearings identified by a viscoelastic model,” *International Journal of Solids and Structures*, vol. 38, no. 1, pp. 53–74, 2001.
- [23] C. G. Koh and J. M. Kelly, “A simple mechanical model for elastomeric bearings used in base isolation,” *International Journal of Mechanical Sciences*, vol. 30, no. 12, pp. 933–943, 1988.
- [24] J. M. Kelly and D. A. Konstantinidis, *Mechanics of Rubber Bearings for Seismic and Vibration Isolation*. John Wiley & Sons, Ltd., 2011.
- [25] F. McKenna and G. L. Fenves, “Open system for earthquake engineering simulation (OpenSees).” [Online]. Available: <http://opensees.berkeley.edu/OpenSees/home/about.php>, 2006.
- [26] M. Brescia, R. Landolfo, O. Mammana, F. Iannone, V. Piluso, and G. Rizzano, “Preliminary results of an experimental program on the cyclic response and rotation capacity of steel members,” in *6th International Specialty Conference on Behaviour of Steel Structures in Seismic Areas*, (Philadelphia), pp. 971–976, 2009.
- [27] A. N. Gent, *Engineering with Rubber*. Munich: Carl Hanser Verlag, 2nd ed., 2001.
- [28] J. H. Hodgson, “Seismic probably map for canada,” Tech. Rep. 22, National

Research Council, Ottawa, 1956.

- [29] CSA, *S16-14: Design of Steel Structures*. Canadian Standards Association, Mississauga, 2014.
- [30] CISC, *Handbook of Steel Construction*. Canadian Institute of Steel Construction, Toronto, 10th ed., 2011.
- [31] PEER, “PEER Ground motion database.” [Online]. Available: <http://ngawest2.berkeley.edu/>, 2013.
- [32] ASCE, *Minimum Design Loads for Buildings and Other Structures*. American Society of Civil Engineers, Reston, 2006.
- [33] ASTM, *A370: Standard Test Methods and Definitions for Mechanical Testing of Steel Products*. American Society for Testing and Materials, West Conshohocken, 2015.

APPENDIX A: SOURCE CODE FOR THE OPENSEES ELEMENT

The source code for the element created for use with OpenSees was written in C++ and contains two files. The first file, `ElastomericRotation.h`, is a header file which defines all of the methods and variables required to set up the element. The second file, `ElastomericRotation.cpp`, is an implementation file which details the functions of all the methods and assigns values to the variables defined in the header file. The following is a copy of the header file, followed by the implementation file.

```

1 /* ***** **
2 **   OpenSees – Open System for Earthquake Engineering Simulation   **
3 **   Pacific Earthquake Engineering Research Center                 **
4 **                                                                 **
5 **                                                                 **
6 ** (C) Copyright 1999, The Regents of the University of California **
7 ** All Rights Reserved.                                           **
8 **                                                                 **
9 ** Commercial use of this program without express permission of the **
10 ** University of California, Berkeley, is strictly prohibited. See **
11 ** file 'COPYRIGHT' in main directory for information on usage and **
12 ** redistribution, and for a DISCLAIMER OF ALL WARRANTIES.      **
13 **                                                                 **
14 ** Developed by:                                                 **
15 **   Frank McKenna (fmckenna@ce.berkeley.edu)                   **
16 **   Gregory L. Fenves (fenves@ce.berkeley.edu)                 **
17 **   Filip C. Filippou (filippou@ce.berkeley.edu)               **
18 **                                                                 **
19 ** ***** */
20
21 // $Revision: 1.0 $
22 // $Date: 2014/08/21 14:19:50 $
23 // $Source: /usr/local/cvs/OpenSees/SRC/element/bearing/ElastomericRotation.h,v $
24
25 #ifndef ElastomericRotation_h
26 #define ElastomericRotation_h
27
28 // Written: Adrian Crowder
29 // Version: 1.0
30 //
31 // Created: August 21, 2014
32 // Updated: August 21, 2014
33 //
34 // Purpose: This file contains the class definition for ElastomericRotation.
35 // ElastomericRotation is an elastomeric bearing with coupled rotation and
36 // shear terms, and also accounts for P-Delta effects.
37 //
38 // What: "@(#) ElastomericRotation.h, revA"

```

```
39
40 #include <Element.h>
41 #include <Node.h>
42 #include <Matrix.h>
43 #include <Vector.h>
44
45 class Channel;
46 class Information;
47 class Response;
48 class Renderer;
49
50 class ElastomericRotation : public Element
51 {
52 public:
53     // constructors
54     ElastomericRotation(int tag, int iNd, int jNd, double r, double t,
55         double tr, double h, double G, double P, double K = 0.0);
56
57     ElastomericRotation();
58
59     // destructor
60     ~ElastomericRotation();
61
62     const char *getClassType(void) const { return "ElastomericRotation"; };
63
64     // public methods to obtain information about dof & connectivity
65     int getNumExternalNodes(void) const;
66     const ID &getExternalNodes(void);
67     Node **getNodePtrs(void);
68     int getNumDOF(void);
69     void setDomain(Domain *theDomain);
70
71     // public methods to set the state of the element
72     int commitState(void);
73     int revertToLastCommit(void);
74     int revertToStart(void);
75     int update(void);
76
77     // public methods to obtain stiffness
78     const Matrix &getTangentStiff(void);
79     const Matrix &getInitialStiff(void);
80     const Matrix &getMass(void);
81
82     // public method to obtain resisting force
83     const Vector &getResistingForce(void);
84
85     // public methods for output
86     int sendSelf(int commitTag, Channel &theChannel);
87     int recvSelf(int commitTag, Channel &theChannel, FEM_ObjectBroker &theBroker);
88     void Print(OPS_Stream &s, int flag =0);
89     int displaySelf(Renderer &theViewer, int displayMode, float fact);
90
91     Response *setResponse(const char **argv, int argc, OPS_Stream &s);
92     int getResponse(int responseID, Information &eleInformation);
93
94 protected:
95
96 private:
97     Matrix calcK1(double P);
98     Matrix MMMult(const Matrix A, const Matrix B);
99     Vector MVMult(const Matrix M, const Vector V);
100     Matrix MTrans(const Matrix A);
101
102     double G, K, r, t, tr, h;
```

```

103 double GAs, EIs;
104 double L; // Length of element (between nodes)
105
106 static Matrix T; // Transformation matrix
107 static Matrix Ti; // Inverted transformation matrix
108
109 static Vector ug; // global displacements
110 static Matrix Kg; // global stiffness matrix
111 static Vector Rg; // global force vector
112
113 static Vector ul; // local displacements
114 static Matrix Kl; // Local stiffness matrix
115 static Vector Rl; // local force vector
116
117 double Pl; // Local axial load
118
119 Node *theNodes[2];
120 ID externalNodes;
121 };
122 #endif

```

```

1 /* ***** **
2 ** OpenSees – Open System for Earthquake Engineering Simulation **
3 ** Pacific Earthquake Engineering Research Center **
4 ** **
5 ** **
6 ** (C) Copyright 1999, The Regents of the University of California **
7 ** All Rights Reserved. **
8 ** **
9 ** Commercial use of this program without express permission of the **
10 ** University of California, Berkeley, is strictly prohibited. See **
11 ** file 'COPYRIGHT' in main directory for information on usage and **
12 ** redistribution, and for a DISCLAIMER OF ALL WARRANTIES. **
13 ** **
14 ** Developed by: **
15 ** Frank McKenna (fmckenna@ce.berkeley.edu) **
16 ** Gregory L. Fenves (fenves@ce.berkeley.edu) **
17 ** Filip C. Filippou (filippou@ce.berkeley.edu) **
18 ** **
19 ** ***** */
20
21 // Written: Adrian Crowder
22 // Version: 1.0
23 //
24 // Created: August 21, 2014
25 // Updated: August 21, 2014
26 //
27 // Purpose: This file contains the class definition for ElastomericRotation.
28 // ElastomericRotation is an elastomeric bearing with coupled rotation and
29 // shear terms, and also accounts for P-Delta effects.
30
31
32 // we specify what header files we need
33 #include "ElastomericRotation.h"
34 #include <elementAPI.h>
35 #include <G3Globals.h>
36
37 #include <Information.h>
38 #include <Domain.h>
39 #include <Node.h>
40 #include <Channel.h>
41 #include <Message.h>

```

```
42 #include <FEM_ObjectBroker.h>
43 #include <Renderer.h>
44 #include <ElementResponse.h>
45
46 #include <math.h>
47 #include <stdlib.h>
48 #include <string.h>
49
50 // initialize the class wide variables
51 Matrix ElastomericRotation::T(6, 6);
52 Matrix ElastomericRotation::Ti(6, 6);
53
54 Vector ElastomericRotation::ug(6);
55 Matrix ElastomericRotation::Kg(6, 6);
56 Vector ElastomericRotation::Rg(6);
57
58 Vector ElastomericRotation::ul(6);
59 Matrix ElastomericRotation::Kl(6, 6);
60 Vector ElastomericRotation::Rl(6);
61
62 #ifdef _USRDLL
63 #include <windows.h>
64 #define OPS_Export extern "C" _declspec(dllexport)
65 #elif _MACOSX
66 #define OPS_Export extern "C" __attribute__((visibility("default")))
67 #else
68 #define OPS_Export extern "C"
69 #endif
70
71 static int numElastoRot = 0;
72
73 OPS_Export void *
74 OPS_ElastomericRotation()
75 {
76     // print out a message about who wrote this element & any copyright info wanted
77     if (numElastoRot == 0) {
78         opserr << "\nElastomericRotation element - Written by Adrian Crowder, McMaster
79         University" << endl;
80         opserr << "Copyright 2014\n" << endl;
81         numElastoRot++;
82     }
83
84     Element *theElement = 0;
85
86     int numRemainingArgs = OPS_GetNumRemainingInputArgs();
87     if (numRemainingArgs == 0) { // parallel processing
88         theElement = new ElastomericRotation();
89         return theElement;
90     }
91
92     if ((numRemainingArgs != 9) && (numRemainingArgs != 10)) {
93         opserr << "ERROR - ElastomericRotation not enough args provided, want: element
94         ElastomericRotation tag? iNode? jNode? Radius? t? tr? height? G? <As>\n";
95         numElastoRot++;
96     }
97
98     // get the id and end nodes
99     int iData[3];
100     double dData[7];
101     int numData;
102
103     numData = 3;
104     if (OPS_GetIntInput(&numData, iData) != 0) {
105         opserr << "WARNING invalid element tag or nodes\n";
106     }
107 }
```

```

104     return 0;
105 }
106
107 int eleTag = iData[0];
108
109 numData = 4;
110 if (OPS_GetDoubleInput(&numData, dData) != 0) {
111     opserr << "WARNING error reading dimensions for element " << eleTag << endl;
112     return 0;
113 }
114
115 numData = 1;
116 if (OPS_GetDoubleInput(&numData, &dData[4]) != 0) {
117     opserr << "WARNING error reading shear modulus for element " << eleTag << endl;
118     return 0;
119 }
120
121 numData = 1;
122 if (OPS_GetDoubleInput(&numData, &dData[5]) != 0) {
123     opserr << "WARNING error reading axial load for element " << eleTag << endl;
124     return 0;
125 }
126
127 if (numRemainingArgs == 10) {
128     numData = 1;
129     if (OPS_GetDoubleInput(&numData, &dData[6]) != 0) {
130         opserr << "WARNING error reading bulk modulus for element " << eleTag << endl;
131         return 0;
132     }
133 }
134
135 // now create the bearing and add it to the Domain
136 if (numRemainingArgs == 9) {
137     theElement = new ElastomericRotation(eleTag, iData[1], iData[2],
138         dData[0], dData[1], dData[2], dData[3], dData[4], dData[5]);
139 }
140 else {
141     theElement = new ElastomericRotation(eleTag, iData[1], iData[2],
142         dData[0], dData[1], dData[2], dData[3], dData[4], dData[5], dData[6]);
143 }
144
145 if (theElement == 0) {
146     opserr << "WARNING ran out of memory creating element with tag " << eleTag <<
147     endl;
148     return 0;
149 }
150
151 return theElement;
152 }
153 // typical constructor
154 ElastomericRotation::ElastomericRotation(int tag,
155     int iNd, int jNd,
156     double R, double T, double TR, double H, double g, double p,
157     double k)
158 : Element(tag, 0),
159   externalNodes(2),
160   r(R), t(T), tr(TR), h(H), G(g), Pl(p), K(k)
161 {
162     externalNodes(0) = iNd;
163     externalNodes(1) = jNd;
164
165     // set node pointers to NULL
166     theNodes[0] = 0;

```

```

167   theNodes[1] = 0;
168 }
169
170 // constructor which should be invoked by an FE_ObjectBroker only
171 ElastomericRotation::ElastomericRotation()
172 :Element(0, 0),
173 externalNodes(2),
174 r(0), t(0), tr(0), h(0), G(0), P1(0), K(0)
175 {
176   theNodes[0] = 0;
177   theNodes[1] = 0;
178 }
179
180 // destructor – provided to clean up any memory
181 ElastomericRotation::~ElastomericRotation()
182 {
183   // clean up the memory associated with the element, this is
184   // memory the ElastomericRotation objects allocates and memory allocated
185   // by other objects that the ElastomericRotation object is responsible for
186   // cleaning up, i.e. the MaterialObject.
187 }
188 }
189
190 int
191 ElastomericRotation::getNumExternalNodes(void) const
192 {
193   return 2;
194 }
195
196 const ID &
197 ElastomericRotation::getExternalNodes(void)
198 {
199   return externalNodes;
200 }
201
202 Node **
203 ElastomericRotation::getNodePtrs(void)
204 {
205   return theNodes;
206 }
207
208 int
209 ElastomericRotation::getNumDOF(void) {
210   return 6;
211 }
212
213 void
214 ElastomericRotation::setDomain(Domain *theDomain)
215 {
216   // check Domain is not null – invoked when object removed from a domain
217   if (theDomain == 0) {
218     return;
219   }
220
221   // first ensure nodes exist in Domain and set the node pointers
222   int Ndi = externalNodes(0);
223   int Ndj = externalNodes(1);
224   theNodes[0] = theDomain->getNode(Ndi);
225   theNodes[1] = theDomain->getNode(Ndj);
226
227   if (theNodes[0] == 0) {
228     opserr << "ElastomericRotation::setDomain — Node i: " << Ndi << " does not exist
229     \n";

```

```

230     return; // don't go any further - otherwise segmentation fault
231 }
232
233 if (theNodes[1] == 0) {
234     opserr << "ElastomericRotation::setDomain -- Node j: " << Ndj << " does not exist
235     \n";
236     return; // don't go any further - otherwise segmentation fault
237 }
238
239     // ensure connected nodes have correct number of dof's
240 int dofNdi = theNodes[0]->getNumberDOF();
241 int dofNdj = theNodes[1]->getNumberDOF();
242 if ((dofNdi != 3) || (dofNdj != 3)) {
243     opserr << "ElastomericRotation::setDomain -- 2 dof required at nodes\n";
244     return;
245 }
246
247
248 // call the DomainComponent class method THIS IS VERY IMPORTANT
249 this->DomainComponent::setDomain(theDomain);
250
251
252     // now determine the length & transformation matrix
253 const Vector NdiCrds = theNodes[0]->getCrds();
254 const Vector NdjCrds = theNodes[1]->getCrds();
255
256 double dx = NdjCrds(0) - NdiCrds(0);
257 double dy = NdjCrds(1) - NdiCrds(1);
258
259 L = sqrt(dx*dx + dy*dy);
260
261 if (L == 0.0) {
262     opserr << "WARNING ElastomericRotation::setDomain - ElastomericRotation " << this
263     ->getTag() <<
264     " has zero length\n";
265     return; // don't go any further - otherwise divide by 0 error
266 }
267
268 double cos_th = dx / L;
269 double sin_th = dy / L;
270
271 // set T to a zero matrix first, then fill in needed transformations
272 T.Zero();
273 T(0, 0) = T(3, 3) = cos_th;   T(0, 1) = T(3, 4) = -sin_th;
274 T(1, 0) = T(4, 3) = sin_th;   T(1, 1) = T(4, 4) = cos_th;
275 T(2, 2) = T(5, 5) = 1;
276
277 // Transformation inverse equal to transpose
278 Ti = MTrans(T);
279
280 // Set up Pi
281 double PI = acos(-1.0);
282
283
284 // Calculate shear stiffness
285 GAs = PI * G * pow(r, 2.0) * (h / tr);
286
287
288 // Calculate flexural stiffness, if K was not given then assume incompressible
289 // material
290 if (K == 0) {
291     EIs = (PI * G * pow(r, 6.0)) / (8 * pow(t, 2.0)) * (h / tr);

```

```

291 }
292 else {
293     EIs = (PI * G * pow(r, 6.0)) / (8 * pow(t, 2.0)) * (1 - (3 * G * pow(r, 2.0)) /
294         (4 * K * pow(t, 2.0))) * (h / tr);
295 }
296
297 // Calculate the stiffness matrices
298 K1 = calcK1(P1);
299 Kg = MMMult(T, MMMult(K1, Ti));
300 }
301
302 int
303 ElastomericRotation::commitState()
304 {
305     return 0;
306 }
307
308 int
309 ElastomericRotation::revertToLastCommit()
310 {
311     return 0;
312 }
313
314 int
315 ElastomericRotation::revertToStart()
316 {
317     return 0;
318 }
319
320 int
321 ElastomericRotation::update()
322 {
323     // Determine current displacements
324     const Vector NdiDsp = theNodes[0]->getTrialDisp();
325     const Vector NdjDsp = theNodes[1]->getTrialDisp();
326
327     for (int i = 0; i < 3; i++) {
328         ug[i] = NdiDsp[i];
329         ug[i + 3] = NdjDsp[i];
330     }
331
332     ul = MVMult(Ti, ug);
333
334     return 0;
335 }
336
337 const Matrix &
338 ElastomericRotation::getTangentStiff(void)
339 {
340     if (L == 0) { // if there is no length then the transformation matrix is not
341         defined
342         Kg.Zero();
343         return Kg;
344     }
345     return Kg;
346 }
347
348 const Matrix &
349 ElastomericRotation::getInitialStiff(void)
350 {
351     if (L == 0) {
352         Kg.Zero();

```

```

353     return Kg;
354 }
355
356     return Kg;
357 }
358
359 const Matrix &
360 ElastomericRotation::getMass(void)
361 {
362     // no mass
363     K1.Zero();
364     return K1;
365 }
366
367 const Vector &
368 ElastomericRotation::getResistingForce()
369 {
370     if (L == 0) {
371         Rg.Zero();
372         return Rg;
373     }
374
375     this->update();
376
377     R1 = MVMult(K1, ul);
378     Rg = MVMult(Kg, ug);
379
380     return Rg;
381 }
382
383 int
384 ElastomericRotation::sendSelf(int commitTag, Channel &theChannel)
385 {
386     return -1; // no database or parallel processing
387 }
388
389 int
390 ElastomericRotation::recvSelf(int commitTag, Channel &theChannel, FEM_ObjectBroker &
391     theBroker)
392 {
393     return -1; // no database or parallel processing
394 }
395 void
396 ElastomericRotation::Print(OPS_Stream &s, int flag)
397 {
398     this->getResistingForce();
399     s << "\nElastomericRotation: " << this->getTag() << endl;
400     s << "\tConnected Nodes: " << externalNodes(0) << " " << externalNodes(1) << endl;
401     s << "\tEnd 1 Forces (P V M): " << R1[0] << " " << R1[1] << " " << R1[2] << endl;
402     s << "\tEnd 2 Forces (P V M): " << R1[3] << " " << R1[4] << " " << R1[5] << endl;
403 }
404
405 int
406 ElastomericRotation::displaySelf(Renderer &theViewer, int displayMode, float fact)
407 {
408     // first determine the end points of the beam based on
409     // the display factor (a measure of the distorted image)
410     const Vector &end1Crd = theNodes[0]->getCrds();
411     const Vector &end2Crd = theNodes[1]->getCrds();
412
413     static Vector v1(3);
414     static Vector v2(3);
415

```

```

416
417 if (displayMode >= 0) {
418     const Vector &end1Disp = theNodes[0]->getDisp();
419     const Vector &end2Disp = theNodes[1]->getDisp();
420
421     for (int i = 0; i < 2; i++) {
422         v1(i) = end1Crd(i) + end1Disp(i)*fact;
423         v2(i) = end2Crd(i) + end2Disp(i)*fact;
424     }
425 }
426 else {
427     int mode = displayMode * -1;
428     const Matrix &eigen1 = theNodes[0]->getEigenvectors();
429     const Matrix &eigen2 = theNodes[1]->getEigenvectors();
430     if (eigen1.noCols() >= mode) {
431         for (int i = 0; i < 2; i++) {
432             v1(i) = end1Crd(i) + eigen1(i, mode - 1)*fact;
433             v2(i) = end2Crd(i) + eigen2(i, mode - 1)*fact;
434         }
435     }
436     else {
437         for (int i = 0; i < 2; i++) {
438             v1(i) = end1Crd(i);
439             v2(i) = end2Crd(i);
440         }
441     }
442 }
443
444 static Vector p1(3);
445 static Vector p2(3);
446 static Vector p3(3);
447 static Vector p4(3);
448
449 p1(0) = v1(0) - r*v1(2)*T(0, 0) - r*T(0, 1);
450 p1(1) = v1(1) + r*T(0, 0) - r*v1(2)*T(0, 1);
451 p1(2) = v1(2);
452
453 p2(0) = v1(0) + r*v1(2)*T(0, 0) + r*T(0, 1);
454 p2(1) = v1(1) - r*T(0, 0) + r*v1(2)*T(0, 1);
455 p2(2) = v1(2);
456
457 p3(0) = v2(0) - r*v2(2)*T(0, 0) - r*T(0, 1);
458 p3(1) = v2(1) + r*T(0, 0) - r*v2(2)*T(0, 1);
459 p3(2) = v2(2);
460
461 p4(0) = v2(0) + r*v2(2)*T(0, 0) + r*T(0, 1);
462 p4(1) = v2(1) - r*T(0, 0) + r*v2(2)*T(0, 1);
463 p4(2) = v2(2);
464
465 int res = 0;
466 res += theViewer.drawLine(p1, p2, 1.0, 1.0);
467 res += theViewer.drawLine(p2, p4, 1.0, 1.0);
468 res += theViewer.drawLine(p4, p3, 1.0, 1.0);
469 res += theViewer.drawLine(p3, p1, 1.0, 1.0);
470 res += theViewer.drawLine(v1, v2, 1.0, 1.0);
471
472 return res;
473 }
474
475 Response *
476 ElastomericRotation::setResponse(const char **argv, int argc, OPS_Stream &output)
477 {
478     Response *theResponse = 0;
479

```

```

480 output.tag("ElementOutput");
481 output.attr("eleType", "ElastomericRotation");
482 output.attr("eleTag", this->getTag());
483 output.attr("node1", externalNodes[0]);
484 output.attr("node2", externalNodes[1]);
485
486 // global forces
487 if (strcmp(argv[0], "force") == 0 || strcmp(argv[0], "forces") == 0 ||
488     strcmp(argv[0], "globalForce") == 0 || strcmp(argv[0], "globalForces") == 0) {
489
490     output.tag("ResponseType", "Px_1");
491     output.tag("ResponseType", "Py_1");
492     output.tag("ResponseType", "Mz_1");
493     output.tag("ResponseType", "Px_2");
494     output.tag("ResponseType", "Py_2");
495     output.tag("ResponseType", "Mz_2");
496
497     theResponse = new ElementResponse(this, 2, Rg);
498
499     // local forces
500 }
501 else if (strcmp(argv[0], "localForce") == 0 || strcmp(argv[0], "localForces") == 0)
502 {
503     output.tag("ResponseType", "N_1");
504     output.tag("ResponseType", "V_1");
505     output.tag("ResponseType", "M_1");
506     output.tag("ResponseType", "N_2");
507     output.tag("ResponseType", "V_2");
508     output.tag("ResponseType", "M_2");
509
510     theResponse = new ElementResponse(this, 3, Rl);
511 }
512
513
514 output.endTag(); // ElementOutput
515
516 return theResponse;
517 }
518
519 int
520 ElastomericRotation::getResponse(int responseID, Information &eleInfo)
521 {
522     this->getResistingForce();
523
524     switch (responseID) {
525     case 1: // stiffness
526         return eleInfo.setMatrix(this->getTangentStiff());
527
528     case 2: // global forces
529         return eleInfo.setVector(this->getResistingForce());
530
531     case 3: // local forces
532         return eleInfo.setVector(Rl);
533
534     default:
535         return -1;
536     }
537 }
538
539 Matrix
540 ElastomericRotation::calcKl(const double P)
541 {
542     Matrix res(6, 6);

```

```

543
544 if (P == 0) { // if P == 0 then this procedure would attempt division by zero
545     opserr << "ElastomericRotation::calcKl — axial load cannot equal zero";
546     res.Zero();
547     return res;
548 }
549
550 // Update alpha and beta parameters
551 double alpha = sqrt(P*(P + GAs) / (GAs*EIs));
552 double beta = GAs / (P + GAs);
553
554 double ab = alpha*beta;
555 double lam = tan(alpha*h / 2);
556 double trm1;
557
558 double PI = acos(-1.0);
559
560 trm1 = 3 * PI*G*pow(r, 4) / (2 * tr * pow(t, 2));
561
562 double frontFac = P / (2 * lam - ab*h);
563
564 res(0, 0) = trm1;
565 res(0, 1) = 0;
566 res(0, 2) = 0;
567 res(0, 3) = -trm1;
568 res(0, 4) = 0;
569 res(0, 5) = 0;
570
571 res(1, 1) = frontFac*ab;
572 res(1, 2) = frontFac*lam;
573 res(1, 3) = 0;
574 res(1, 4) = -frontFac*ab;
575 res(1, 5) = frontFac*lam;
576
577 res(2, 2) = frontFac*(1/ab - h/tan(alpha*h));
578 res(2, 3) = 0;
579 res(2, 4) = -frontFac*lam;
580 res(2, 5) = frontFac*(-1/ab + h/sin(alpha*h));
581
582 res(3, 3) = trm1;
583 res(3, 4) = 0;
584 res(3, 5) = 0;
585
586 res(4, 4) = frontFac*ab;
587 res(4, 5) = -frontFac*lam;
588
589 res(5, 5) = frontFac*(1 / ab - h / tan(alpha*h));
590
591
592 // Fill in remaining terms from symmetry
593 res(1, 0) = res(0, 1);
594
595 res(2, 0) = res(0, 2);
596 res(2, 1) = res(1, 2);
597
598 res(3, 0) = res(0, 3);
599 res(3, 1) = res(1, 3);
600 res(3, 2) = res(2, 3);
601
602 res(4, 0) = res(0, 4);
603 res(4, 1) = res(1, 4);
604 res(4, 2) = res(2, 4);
605 res(4, 3) = res(3, 4);
606

```

```

607     res(5, 0) = res(0, 5);
608     res(5, 1) = res(1, 5);
609     res(5, 2) = res(2, 5);
610     res(5, 3) = res(3, 5);
611     res(5, 4) = res(4, 5);
612
613     return res;
614 }
615
616 Matrix
617 ElastomericRotation::MMMult(const Matrix A, const Matrix B)
618 {
619     int ma = A.noRows();
620     int na = A.noCols();
621     int mb = B.noRows();
622     int nb = B.noCols();
623
624     Matrix result(ma, nb);
625
626     if (na != mb) {
627         opserr << "ElastomericRotation::MMMult — Invalid matrix dimensions";
628         result.Zero();
629         return result;
630     }
631
632     double sum;
633     for (int m = 0; m < ma; m++) { // for each row
634         for (int n = 0; n < nb; n++) { // for each column
635             sum = 0.0;
636
637             for (int i = 0; i < na; i++) { // dot product
638                 sum += A(m, i)*B(i, n);
639             }
640             result(m, n) = sum;
641         }
642     }
643
644     return result;
645 }
646
647 Vector
648 ElastomericRotation::MVMult(const Matrix M, const Vector V)
649 {
650     int mm = M.noRows();
651     int nm = M.noCols();
652     int mv = V.Size();
653
654     Vector result(mv);
655
656     if (nm != mv) {
657         opserr << "ElastomericRotation::MVMult — Invalid matrix and vector dimensions";
658         result.Zero();
659         return result;
660     }
661
662     double sum;
663     for (int m = 0; m < mv; m++) { // for each row
664         sum = 0.0;
665
666         for (int i = 0; i < nm; i++) { // dot product
667             sum += M(m, i)*V(i);
668         }
669
670         result(m) = sum;

```

```
671     }
672
673     return result;
674 }
675
676 Matrix
677 ElastomericRotation::MTrans(const Matrix A)
678 {
679     int ma = A.noRows();
680     int na = A.noCols();
681
682     Matrix res(na, ma);
683
684     for (int m = 0; m < ma; m++) {
685         for (int n = 0; n < na; n++) {
686             res(n, m) = A(m, n);
687         }
688     }
689     return res;
690 }
```

APPENDIX B: COUPON TESTING RESULTS

Coupons specimens were taken from each column in the experimental program and manufactured according to ASTM A370 specifications for mechanical testing of steel products [33]. All coupons were milled to the specified dimensions for a plate section with a gauge length of 50 mm, and underwent tensile testing to determine the yield strength and the nonlinear transition. Figures B.1, B.2, B.3, and B.4 show the results from the testing of the HSS127x127x8.0, HSS102x102x8.0, HSS76x76x4.8, and HSS64x64x4.8 coupons, respectively. Test results were used to calibrate the stress-strain behaviour modelled in the numerical simulations, and comparison with numerical results are also included in the figure. Parameters used to calibrate the Giuffr -Menegotto-Pinto model for each coupon include the strain hardening ratio b , and three shaping parameters, $R0$, $cR1$, and $cR2$. The values used for each parameter are shown to the right of each figure.

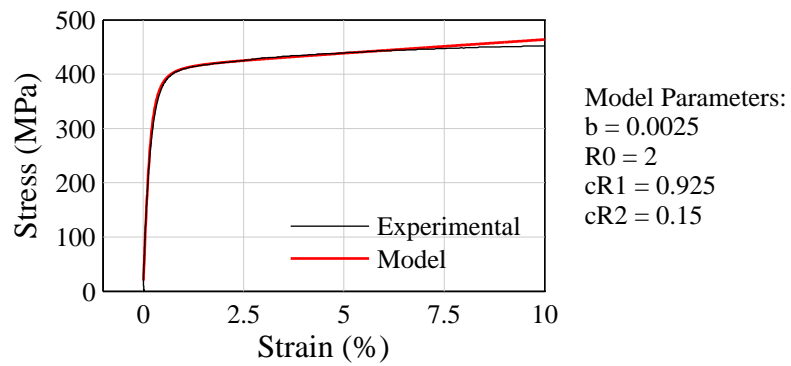


Figure B.1: Results from the HSS127x127x8.0 coupon testing

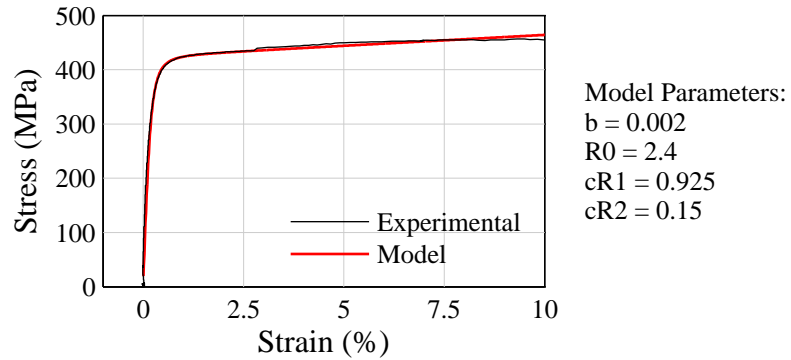


Figure B.2: Results from the HSS102x102x8.0 coupon testing

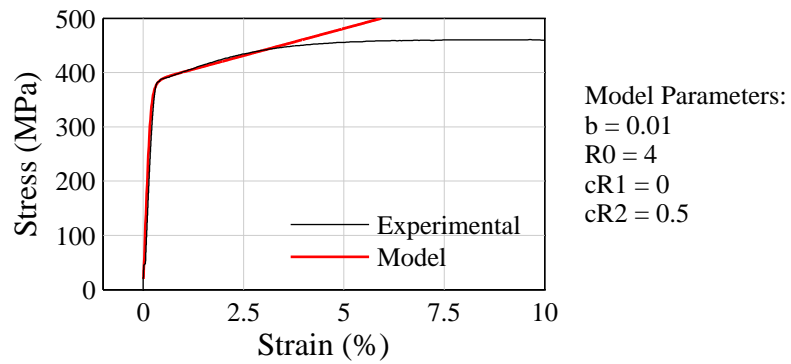


Figure B.3: Results from the HSS76x76x4.8 coupon testing

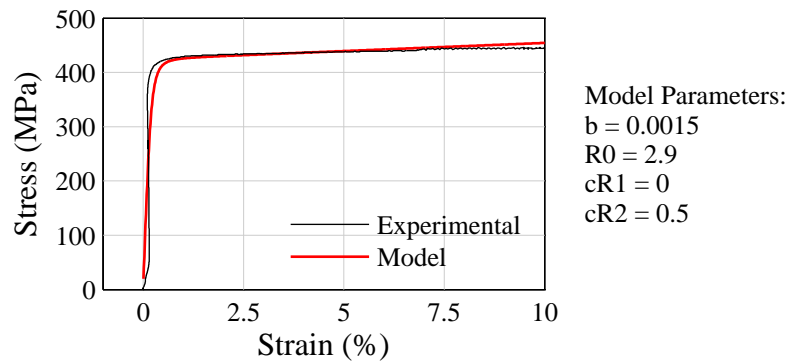


Figure B.4: Results from the HSS64x64x4.8 coupon testing

APPENDIX C: SUPPLEMENTARY EXPERIMENTAL INFORMATION

Table C.1: Instrumentation channels

Channel	Instrument	Measure
101	String pot	Horizontal actuator displacement
102	String pot	Column lateral displacement
103	LVDT	West vertical actuator displacement
104	LVDT	East vertical actuator displacement
105	Load cell	Horizontal actuator force
106	Load cell	West vertical actuator force
107	Load cell	East vertical actuator force
108	Load cell	South-West force under uniaxial table
109	Load cell	North-West force under uniaxial table
110	Load cell	North-East force under uniaxial table
111	Load cell	South-East force under uniaxial table
112	Inclinometer	Rotation of column-bearing interface
201	Strain gauge	West strain from set 1
202	Strain gauge	East strain from set 1
203	Strain gauge	West strain from set 2
204	Strain gauge	East strain from set 2
205	Strain gauge	West strain from set 3
206	Strain gauge	East strain from set 3
207	Strain gauge	West strain from set 4
208	Strain gauge	East strain from set 4
209	Strain gauge	West strain from set 5
210	Strain gauge	East strain from set 5

Table C.2: Commercial instrumentation and equipment used in the experimental setup

Instrument	Company	Model
Load cells	Interface	1020
Strain gauges	Micro-Measurements	250LW-120
Inclinometer	Measurement Specialties	NS-5/DMG2-U
Vertical actuators	Shur-Lift	4x18 Utility
Horizontal actuator	Shur-Lift	2.5x12 Implement
Linear Sliders	THK	SHS 30LC + 1000L
Data acquisition	Agilent	34970A
Control system	MTS	FlexTest GT